

# A finite volume framework for damage and fracture prediction in wire drawing

Andrew Whelan<sup>1,2,3,4</sup>, Tian Tang<sup>5</sup>, Vikram Pakrashi<sup>1,2,3,4</sup>,  
Philip Cardiff<sup>1,2,3,4,6\*</sup>

<sup>1</sup>\*School of Mechanical and Materials Engineering, University College Dublin, Ireland.

<sup>2</sup>SFI MaREI Centre, University College Dublin, Ireland.

<sup>3</sup>UCD Centre for Mechanics, University College Dublin, Ireland.

<sup>4</sup>Bekaert University Technology Centre, University College Dublin, Ireland.

<sup>5</sup>NV Bekaert SA, Kortrijk, Belgium.

<sup>6</sup>SFI I-Form Centre, University College Dublin, Ireland.

\*Corresponding author. E-mail: philip.cardiff@ucd.ie

## Abstract

This article presents the implementation of the canonical Lemaitre and Gurson-Tvergaard-Needleman (GTN) damage models and a more recent phase-field type model within a Lagrangian, geometrically nonlinear, cell-centred finite volume framework. The proposed segregated solution procedure uses Picard-type defect (deferred) outer corrections, where the primary unknowns are cell-centre displacements and pressures. Spurious zero-energy modes (numerical oscillations in displacement and pressure) are avoided by introducing stabilisation (smoothing) diffusion terms to the pressure and momentum equations. Appropriate scaling of the momentum “Rheie-Chow” stabilisation term is shown to be important in regions of plasticity and damage. To accurately predict damage and fracture in wire drawing where hydrostatic pressure is high, novel variants of the Lemaitre model with crack-closure and triaxiality effects are proposed. The developed methods are validated against the *flat notched bar* and *notched round bar* experimental cases, and subsequently applied to the analysis of axisymmetric wire drawing. It is shown that the proposed finite volume approach provides a robust basis for predicting damage in wire drawing, where the proposed novel Lemaitre model with crack-closure effects was shown to be the most suitable for predicting experimentally observed fracture in wire drawing.

**Keywords:** finite volume method, damage, fracture, Lemaître, Gurson-Tvergaard-Needleman, phase field model, OpenFOAM

## 1 Introduction

Numerical simulations of ductile fracture are of great interest in industries such as aerospace [1, 2], automotive [3–6], nuclear [7], and metal forming [8–13] to predict where and when damage or fracture will occur. The availability of computational predictive tools allows for substantial savings in the cost of experiments and design optimisation. In this work, the drawing of high-carbon steel wire products is the primary interest [11, 12]. The drawing process can often lead to the development of defects and even fracture during production. By improving understanding of how and why fracture occurs, processes can be optimised to ensure the resulting product is as robust as possible.

A computational model for ductile fracture should predict several features, such as the stress and strain distribution, damage origination and propagation, and the resulting loss of load-carrying capacity. In the review of Besson [14], fracture models were classified into global and local approaches. The Rice  $J$ -integral model is the canonical global approach. This approach suffers from limitations, however, such that it cannot predict crack initiation and propagation, and the  $J$ -integral is also not a material property as it strongly depends on the specimen geometry [15]. These problems were rectified by the  $J$ - $Q$  integral approach; however, this approach, in turn, has the limitation that it does not apply to complex geometries [16]. Further developments in this family of models, such as the critical crack tip opening displacement or crack tip opening angle, share the same limitations [17, 18]. These models have been implemented in finite element solvers with remeshing techniques needed to model the crack propagation.

The limitations of the global approach have led to the development of local approaches. In these approaches, a more physically detailed approach is used to characterise the fracture zone. These models can, in turn, be split into surface models (cohesive zone models), where fracture occurs on a surface, and volume models, where damage or degradation occurs in a volume. A limitation of cohesive zone models is that they often require a pre-defined crack path and typically exhibit strong mesh dependency. With these limitations in mind, this work focusses on the volume or *continuum* damage mechanics approaches, stemming from the work of Lemaître [19, 20], and micro-mechanical approaches, as originally proposed by Gurson-Tvergaard-Needleman (GTN) [21, 22]. A review of these approaches is left to Section 3. Within the past 15 years an alternative volume ductile damage model has emerged, known as the phase field model approach [23–27]. This approach involves diffusing the sharp crack over a continuum. Models of this form are also implemented in this work and are described in Section 3.

In recent years, there has been an increasing interest in exploring the finite volume method for structural application and the interested reader is directed to a recent review by Cardiff and Demirdžić [28]. While the volume damage models have been implemented within finite element frameworks, they have seen little attention within the finite volume community. As shown in this

work, the segregated Picard iteration solution methodology, which is commonly employed in the finite volume method, demonstrates favourable convergence properties for the highly nonlinear material behaviour experienced in wire drawing.

Although both Eulerian and Lagrangian approaches have been adopted for metal forming, the Lagrangian approach is now commonly favoured due to its ability to easily capture elastic effects, e.g. residual stresses and *spring back*, notwithstanding its limitation of mesh deterioration for severe deformations. Nonetheless, for continuous processes such as wire drawing, Lagrangian approaches require the user to select a sufficiently long initial domain (e.g., initial wire length) so that steady-state phenomena of interest can be examined. Eulerian approaches do not have such a limitation as the workpiece *inlet* and *outlet* (i.e., wire upstream and downstream boundaries) are static in space. To combine the advantages of both, the current work proposes a Lagrangian approach with novel Eulerian-style boundary conditions, which allow the wire upstream and downstream boundaries to stay fixed in space.

Three main contributions are proposed in this work: (i) Nascent damage model implementations within a cell-centred finite volume framework, including a novel Lemaitre damage formulation for wire drawing; (ii) Eulerian-style boundary conditions for continuous forming processes, where mesh layers are added and removed at the workpiece upstream and downstream boundaries. (iii) A segregated large strain pressure-displacement finite volume formulation, where scaled Rhee-Chow stabilisation terms are proposed for quelling pressure oscillations, while minimising over-smoothing of the damage fields. All implementations are performed in the solids4foam toolbox [29, 30] for the open-source C++ software OpenFOAM, building on previous work related to metal forming [11, 13]. All related code and cases are publicly shared on GitHub at <http://github.com/awhelanUCD/solids4foam>.

The remainder of the paper is organised as follows: Section 2 describes the mathematical model and presents the finite volume numerical method, where details of the elastoplastic damage laws are left to Section 3. The implemented damage procedures are verified in Section 4, and applied to wire drawing in Section 5. The article ends with a summary of the main conclusions.

## 2 Mathematical Model and Numerical Methods

This section outlines the Lagrangian large strain, finite volume methodology, where details of the constitutive laws are left to Section 3.

### 2.1 Linear momentum conservation

The dynamic, Lagrangian, strong integral form of linear momentum conservation for a body  $\Omega$ , bounded by a surface  $\Gamma$  with outwards pointing normal  $\mathbf{n}$ , can be expressed in *total* Lagrangian form as

$$\int_{\Omega_o} \rho_o \frac{\partial^2 \mathbf{u}}{\partial t^2} d\Omega_o = \oint_{\Gamma_o} (\mathbf{J} \mathbf{F}^{-T} \cdot \mathbf{n}_o) \cdot \boldsymbol{\sigma} d\Gamma_o \quad (1)$$

or equivalently in *updated* Lagrangian form as

$$\int_{\Omega_u} \frac{\partial}{\partial t} \left( \rho_u \frac{\partial \mathbf{u}}{\partial t} \right) d\Omega_u = \oint_{\Gamma_u} (j \mathbf{f}^{-T} \cdot \mathbf{n}_u) \cdot \boldsymbol{\sigma} d\Gamma_u \quad (2)$$

where  $\rho$  is the density,  $\mathbf{u}$  is the displacement vector,  $\boldsymbol{\sigma}$  is the true (Cauchy) stress, and body forces are neglected. Subscript  $o$  indicates quantities in the initial reference configuration, and subscript  $u$  indicates quantities in the updated configuration. The two forms are connected through Nanson's formula [31], which relate the deformed area vector  $\mathbf{\Gamma}$  with the initial area vector  $\mathbf{\Gamma}_o$ :

$$\mathbf{\Gamma} = J \mathbf{F}^{-T} \cdot \mathbf{\Gamma}_o \quad (3)$$

The deformation gradient is defined as  $\mathbf{F} = \mathbf{I} + (\nabla \mathbf{u})^T$  and its determinant (Jacobian) as  $J = \det(\mathbf{F})$ . The *relative* deformation gradient is given in terms of the displacement increment as  $\mathbf{f} = \mathbf{I} + [\nabla(\Delta \mathbf{u})]^T$  and the relative Jacobian as  $j = \det(\mathbf{f})$ .

Although the total Lagrangian approach is a viable option for wire drawing, the current work adopts the updated Lagrangian approach as developing Eulerian-type upstream and downstream conditions (Section 2.4) is conceptually easier in an updated Lagrangian formulation.

The definition of the true stress in Equations 1 and 2 comes from the constitutive law, as is described in Section 3.

## 2.2 Solution Domain Discretisation

The solution domain is discretised in space and time. The total specified simulation time is divided into a finite number of time increments  $\Delta t$ , and the discretised governing momentum equation is solved in a time-marching manner.

The space domain is divided into a finite number of contiguous convex polyhedral cells. The proposed solution discretisation follows closely the approach of Cardiff et al. [13]; consequently, only an overview of the final discretised form of equations and adopted solution algorithm are given below.

To facilitate the use of a segregated solution algorithm, the surface forces term (term on the right-hand side of Equation 2) is split into explicit and implicit components:

$$\begin{aligned} \int_{\Omega_u} \frac{\partial}{\partial t} \left( \rho_u \frac{\partial \mathbf{u}}{\partial t} \right) d\Omega_u &= \underbrace{\oint_{\Gamma_u} K_{imp} \mathbf{n}_u \cdot \nabla(\Delta \mathbf{u}) d\Gamma_u}_{\text{implicit}} \\ &+ \underbrace{\oint_{\Gamma_u} (j \mathbf{f}^{-T} \cdot \mathbf{n}_u) \cdot \boldsymbol{\sigma} d\Gamma_u - \oint_{\Gamma_u} K_{imp} \mathbf{n}_u \cdot \nabla(\Delta \mathbf{u}) d\Gamma_u}_{\text{explicit}} \end{aligned} \quad (4)$$

where the first term on the right-hand side (Laplacian term) is treated implicitly, and the second and third terms on the right-hand side are treated in a deferred correction manner. Here, by

implicit, we mean that the term contributes coefficients to the resulting linear(-ised) system of equations, while the deferred terms will contribute only to the source of the system of linear equations. The overall procedure is implicit in time in that the time step size is not constrained by the Courant–Friedrichs–Lowy condition. From a deferred (or defect) correction perspective, this Laplacian term can be considered an approximate compact-stencil linearisation of the surface stress term. This allows the coupled vector system to be temporarily decoupled in three scalar component equations. These three scalar component equations can then be solved independently, where outer Picard iterations provide the inter-component coupling. Unlike Newton–Raphson approaches, where quadratic convergence may be expected, linear convergence of the residuals can be expected when using a segregated approach; however, this disadvantage is offset in several ways: (i) an exact Jacobian stiffness matrix need not be assembled, which is often costly; (ii) a material tangent is not required for the material laws, as instead the scalar coefficient  $K_{imp}$  is only required; (iii) outer Picard iterations are less expensive than Newton iterations as the discretised systems are smaller to assemble and quicker to solve; (iv) Picard iterations may provide superior convergence when the solution is far from the asymptotic region, potentially resulting in a more robust approach for highly nonlinear large strain fracture and damage cases. Nonetheless, as noted previously [32], segregated solution procedures can require significantly more outer iterations and exhibit slow convergence relative to coupled approaches, particularly in high aspect ratio linear cases. In the current work,  $K_{imp}$  is chosen following the work of Jasak and Weller [33] as

$$K_{imp} = \frac{4}{3}\mu + \kappa \quad (5)$$

where  $\mu$  is the material shear modulus and  $\kappa$  is the bulk modulus. It should be reinforced that the value of  $K_{imp}$  affects convergence but does not affect the final converged solution – assuming convergence is achieved.

The primary unknown to be solved for is the displacement increment  $\Delta\mathbf{u} = \mathbf{u}^{[m+1]} - \mathbf{u}^{[m]}$  where the superscript  $[m]$  indicates a quantity from the previous time step and  $[m+1]$  a quantity from the current (to be calculated) time step.

The resulting conservation equation (Equation 4) is applied to each cell (control volume) in the computational mesh and discretised in terms of the displacement increment at the cell centre/centroid ( $\Delta\mathbf{u}$ )<sub>P</sub> and at the centres of the neighbouring cells  $N_i$ .

The temporal volume integral term is discretised in space using the mid-point rule and discretised in time using a first-order accurate implicit backward Euler scheme [33]:

$$\begin{aligned} \int_{\Omega_u} \frac{\partial}{\partial t} \left( \rho_u \frac{\partial(\Delta\mathbf{u})}{\partial t} \right) d\Omega_u &\approx \frac{\partial}{\partial t} \left( \rho_u \frac{\partial(\Delta\mathbf{u})}{\partial t} \right)_P \Omega_P \\ &\approx \left( \frac{\rho_u^{[m+1]} \frac{\partial(\Delta\mathbf{u})}{\partial t}^{[m+1]} - \rho_u^{[m]} \frac{\partial(\Delta\mathbf{u})}{\partial t}^{[m]}}{\Delta t} \right)_P \Omega_P \\ &\approx \left[ \frac{\rho_u^{[m+1]} \left( \frac{\Delta\mathbf{u}^{[m+1]} - \Delta\mathbf{u}^{[m]}}{\Delta t} \right) - \rho_u^{[m]} \left( \frac{\Delta\mathbf{u}^{[m]} - \Delta\mathbf{u}^{[m-1]}}{\Delta t} \right)}{\Delta t} \right]_P \Omega_P \\ &\approx \frac{1}{\Delta t^2} \left[ \rho_{u_P}^{[m+1]} \Delta\mathbf{u}_P^{[m+1]} - \left( \rho_{u_P}^{[m+1]} + \rho_{u_P}^{[m]} \right) \Delta\mathbf{u}_P^{[m]} + \rho_{u_P}^{[m]} \Delta\mathbf{u}_P^{[m-1]} \right] \Omega_P \end{aligned}$$

(6)

The  $\mathbf{u}^{[m-1]}$  term is discretised in a similar fashion, noting that  $\mathbf{u}^{[m]} = \mathbf{u}^{[m-1]} + \Delta\mathbf{u}$  in Equation 4. In the cases examined in this work, inertial effects are relatively small, so temporal accuracy is not a concern.

The surface forces Laplacian term (first term on the right-hand side of Equation 4) is discretised using central differencing with over-relaxed non-orthogonal correction [13, 33–36]:

$$\oint_{\Gamma_u} K_{imp} \mathbf{n}_u \cdot \nabla (\Delta\mathbf{u}) d\Gamma_u \approx \sum_{f \in N_f} K_{imp}^f |\Delta_{u_f}| \left( \frac{\Delta\mathbf{u}_{N_f} - \Delta\mathbf{u}_P}{|\mathbf{d}_f|} \right) |\Gamma_{u_f}| + \sum_{f \in N_f} K_{imp}^f \mathbf{k}_{u_f} \cdot [\nabla (\Delta\mathbf{u})]_f |\Gamma_{u_f}| \quad (7)$$

where  $N_f$  represents the set of faces  $f$  in cell  $P$ , and neighbouring cell centre  $N_f$  shares face  $f$  with the cell  $P$ . The over-relaxed orthogonal vector  $\Delta_{u_f} = \frac{\mathbf{d}_{u_f}}{|\mathbf{d}_{u_f}| \mathbf{n}_{u_f}}$  and non-orthogonal correction vector  $\mathbf{k}_{u_f} = \mathbf{n}_{u_f} - \Delta_{u_f}$ , where  $\mathbf{n}_{u_f}$  is the outward-facing unit normal to the face  $f$ . Vector  $\mathbf{d}_{u_f}$  connects the centre of cell  $P$  with the centre of cell  $N_f$  in the updated configuration. The first term on the right-hand side is treated implicitly, while the second term - representing non-orthogonal corrections at the face - is treated in a deferred correction manner.

The remaining surface force terms (second and third terms on the right-hand side of Equation 4) are discretised by assuming that they vary linearly across the face as follows [37]:

$$\oint_{\Gamma_u} (j\mathbf{f}^{-T} \cdot \mathbf{n}_u) \cdot \boldsymbol{\sigma} d\Gamma_u \approx \sum_{f \in N_f} \boldsymbol{\Gamma}_{u_f} \cdot (j\boldsymbol{\sigma}\mathbf{f}^{-T})_f \quad (8)$$

$$\oint_{\Gamma_u} K_{imp} \mathbf{n}_u \cdot \nabla (\Delta\mathbf{u}) d\Gamma_u \approx \sum_{f \in N_f} K_{imp} \boldsymbol{\Gamma}_{u_f} \cdot [\nabla (\Delta\mathbf{u})]_f \quad (9)$$

The terms at a face, indicated by the subscript  $f$ , are calculated by linearly interpolating from the adjacent cell-centres. The cell-centre gradients  $\nabla (\Delta\mathbf{u})$  are determined using a least squares method [37].

All dependent variables must be specified at the initial time. Boundary conditions must be applied to the faces that coincide with the boundary of the solution domain. The discretised expressions on boundary faces are modified to account for either the known displacement components in Dirichlet conditions or the known traction for Neumann conditions. Coulomb friction contact boundaries are handled using an iterative penalty method, as described previously [13, 38]. More recent segment-to-segment finite volume contact procedures could also be used [39, 40].

### 2.2.1 Rhie-Chow Stabilisation

The difference in the computational stencil for the first and third terms on the right-hand side in Equation 4 introduces third-order numerical diffusion to the discretisation, which quells spurious

zero-energy checkerboarding solution oscillations. First introduced by Rhie and Chow [41] for cell-centred finite volume methods, Demirdžić and Muzaferija [42] extended this approach for solid mechanics. In the current approach, the Rhie-Chow stabilisation term  $\mathcal{D}_{\text{Rhie-Chow}}$  takes the following form:

$$\mathcal{D}_{\text{Rhie-Chow}} = \sum_{f \in N_f} K_{imp}^f \left[ |\Delta_f| \frac{\Delta \mathbf{u}_{N_f} - \Delta \mathbf{u}_P}{|\mathbf{d}_f|} - \Delta_f \cdot [\nabla(\Delta \mathbf{u})]_f \right] |\Gamma_{u_f}| \quad (10)$$

which comes from the difference between Equations 7 and 9. The first term on the right-hand side represents a compact stencil (two-node) approximation of the face normal gradient, while the second term represents a larger stencil approximation. These two terms cancel out in the limit of mesh refinement (or if the solution varies linearly); otherwise, they produce a stabilisation effect that tends to smooth the solution fields. As the term reduces at a third-order rate, it does not affect the overall scheme's second-order accuracy.

As shown in Section 4, the magnitude of the Rhie-Chow stabilisation affects the localisation behaviour for damage and fracture mechanics models, with a tendency to artificially *smear* damage fields. Two mitigation strategies are proposed here to produce a modified Rhie-Chow stabilisation  $\hat{\mathcal{D}}_{\text{Rhie-Chow}}$ :

- (a) The Rhie-Chow stabilisation is scaled by a global scalar constant  $0 \leq \mathcal{R}$  supplied by the user:

$$\hat{\mathcal{D}}_{\text{Rhie-Chow}} = \mathcal{R} \mathcal{D}_{\text{Rhie-Chow}} \quad (11)$$

- (b) The Rhie-Chow stabilisation is scaled by a global scalar constant in addition to a damage-dependent field:

$$\hat{\mathcal{D}}_{\text{Rhie-Chow}} = \mathcal{R}(1 - D)^2 \mathcal{D}_{\text{Rhie-Chow}} \quad (12)$$

In the first approach, the smoothing effect is reduced globally, lessening the smearing of damage fields; however, this approach's disadvantage is that solution convergence is slowed as the stabilisation term is reduced in magnitude everywhere. In addition, numerical oscillations are more likely to appear, particularly in regions undergoing purely elastic deformation where no dissipation mechanisms exist. In the second approach, a damage variable  $0 < D \leq 1$  (to be introduced in Section 3) reduces the smoothing effect only in regions of damage. The effect of these proposed modifications is examined in Section 4. Although the purpose of the proposed modifications is to reduce the amount of stabilisation,  $\mathcal{R}$  is not limited to be less than unity and hence can be used to increase the amount of stabilisation if desired.

### 2.2.2 Hydrostatic Pressure Calculation

Displacement-only formulations are known to be susceptible to numerical hydrostatic pressure oscillations in regions of large isochoric plastic strains. In Cardiff et al. [13], it was proposed to smooth the relative deformation gradient Jacobian field  $j$ . In contrast, the current approach proposes to decompose the stress tensor into deviatoric and volumetric terms,  $\sigma = \text{dev}(\sigma) - p\mathbf{I}$ ,

and solve a smoothed pressure Poisson equation:

$$p = \hat{p} + \mathcal{D}_{\text{Rhie-Chow}}^p \quad (13)$$

where  $\hat{p}$  is the hydrostatic pressure calculated directly from the displacement field, e.g.  $\hat{p} = -1/J[\kappa \text{tr}(\boldsymbol{\epsilon})]$ . The Rhie-Chow *pressure* stabilisation term  $\mathcal{D}_{\text{Rhie-Chow}}^p$  is discretised according to Equation 10 with the displacement increment  $\Delta\mathbf{u}$  replaced by the pressure  $p$ . As in the case of the discretised momentum equation, the magnitude of the Rhie-Chow stabilisation term can be controlled with a global scale constant  $0 \leq \mathcal{R}_p$  supplied by the user. The effect of the Rhie-Chow stabilisation term here is to smooth out any pressure oscillations. The final stabilised form of the pressure Poisson equation is

$$p - \mathbb{D}\nabla^2 p = \hat{p} - \nabla \cdot (\mathbb{D}\nabla p) \quad (14)$$

where the terms on the left-hand side are discretised implicitly, and the terms on the right-hand side are discretised using deferred corrections, following similar methods to Equations 6 and 7. The second terms on the left and right-hand sides come from the Rhie-Chow stabilisation. The described approach is similar to the formulation proposed by Bijeljina et al. [43–46] for incompressibility, quasi-incompressibility and elastoplasticity. The scalar coefficient  $\mathbb{D}$  ensures the stabilisation is scaled appropriately. Following a similar approach to SIMPLE-type computational fluid dynamic procedures, this term is calculated for a cell  $P$  in terms of the momentum equation diagonal coefficient (first term on the right-hand side of Equation 7):

$$\mathbb{D} = \mathcal{R}_p K_{imp} \Omega_P \sum_{f \in N_f} \frac{|\mathbf{d}_f|}{|\boldsymbol{\Delta}_f| |\boldsymbol{\Gamma}_{u_f}|} \quad (15)$$

As the pressure fields are typically relatively smooth, the predictions have been found to be relatively insensitive to the value of  $\mathcal{R}_p$ , where order of magnitude changes produce minimal effects on the results. Values in the range  $1 \leq \mathcal{R}_p \leq 10^3$  are suitable for the types of cases examined in this work.

## 2.3 Solution Algorithm

The linear momentum equation is discretised for each control volume  $P$  in component form, and a linear algebraic equation of the following form is assembled [33]:

$$a_p \Delta u_p^i + \sum_{f \in N_f} a_n \Delta u_{N_f}^i = b_p^i \quad (16)$$

where  $a_p$  is the scalar central coefficient,  $a_n$  are the scalar coefficients associated with the centre of neighbouring cells,  $\Delta u_p^i$  is the  $i^{th}$  component of the displacement increment at cell  $P$ ,  $\Delta u_{N_f}^i$  is the  $i^{th}$  component of the displacement increment at neighbouring cell  $N_f$ , and  $b_p^i$  is  $i^{th}$  component of the source vector contribution.

These linear algebraic equations are then assembled for all control volumes, creating a system of linear algebraic equations for each direction  $i$ :

$$[\mathbf{K}] [\mathbf{u}] = [\mathbf{f}] \quad (17)$$

where  $[\mathbf{K}]$  is an  $M \times M$  sparse, symmetric coefficient matrix containing the coefficients from the implicit operators, with  $M$  being the total number of cells. The matrix  $[\mathbf{K}]$  is the same for each direction before boundary condition contributions are included, meaning the matrix need only be formed once and stored. The solution vector  $[\mathbf{u}]$  contains a component (e.g.,  $x$ ,  $y$ , or  $z$ ) of the unknown cell-centre displacement increments  $\Delta\mathbf{u}$ , and  $[\mathbf{f}]$  is the source term containing a component of the deferred correction terms. A similar scalar system is formed and solved for the hydrostatic pressure (Equation 14) during the stress calculation.

As noted in Section 2.2, a segregated solution algorithm is employed where the governing vector momentum equation is temporarily decoupled and three scalar equations are solved; outer Picard iterations at each time step provide the inter-equation coupling.

The *inner* linear sparse system is iteratively solved using an incomplete Cholesky preconditioned conjugate gradient method [47]. As noted in previous articles on segregated methods, the inner system need not be solved to a tight tolerance as coefficients and source terms are approximated from the previous increment; a reduction in the residuals of one order of magnitude is typically sufficient. The outer iterations are performed until the predefined tolerance, typically  $1 \times 10^{-6}$ , has been achieved [13].

In the current updated Lagrangian approach, the mesh is moved to the deformed configuration at the end of each time step rather than after each outer iteration. Since the displacements are calculated at the cell centres, a linear least-squared method is employed here [13] to interpolate the displacement increments to the mesh vertices, allowing the mesh to be moved.

The procedures have been implemented and publicly shared within the solids4foam toolbox [29, 30] of the open-source OpenFOAM software.

Algorithm 1 shows an overview of the solution algorithm.

---

**Algorithm 1:** Solution Procedure

---

```

for all time steps do
    while convergence not reached do
        - Discrete governing system (Equation 4) for each cell, using Equations 5-10, in terms of  $\Delta\mathbf{u}$ 
        - Assemble the discretised equations for all cells into three scalar linear systems (Equation 17)
        - Solve the three scalar linear systems in terms of cell-centred displacement increments  $\Delta\mathbf{u}$ 
        - Update/reconstruct the kinematics:  $\nabla(\Delta\mathbf{u})$ ,  $\mathbf{F}$ ,  $J$ ,  $\mathbf{f}$ ,  $j$ 
        - Update the stress ( $\sigma$ ) at the cell-centres using the chosen material law
        - Update the Rhee-Chow stabilisation:  $\hat{\mathcal{D}}_{\text{Rhee-Chow}}$ 
    end while
    - Interpolate cell-centre displacement increments to the vertices
    - Move mesh to the deformed configuration using the vertex displacement increments, incorporating
      layer addition/removal (Section 2.4)
end for

```

---

## 2.4 Eulerian-Type Layer Addition and Removal Boundaries

Steady-state behaviour is typically the primary interest in wire drawing and other continuous forming approaches. Eulerian approaches are a natural choice but are not commonly employed when elastic phenomena (e.g. spring back, residual stresses) are important. When simulating wire drawing using a Lagrangian approach, a naïve approach is to simulate a workpiece segment that is *long enough* to allow steady-state to be reached. The disadvantage of this approach is that computational cost is inflated by the portion of the workpiece domain primarily undergoing rigid-body translation, which may be large relative to the region actively undergoing plastic deformations.

To overcome this disadvantage, the current work proposes Eulerian-type layer addition and removal conditions for the workpiece upstream and downstream boundaries. The approach involves fixing the workpiece (e.g., wire) upstream and downstream mesh boundaries in space during the mesh motion at the end of each time step. As cells at the upstream boundary become elongated, layers of new cells are added. Similarly, cells are removed as they become compressed near the downstream patch. In this way, the length of the workpiece domain remains fixed (like an Eulerian approach), but a traditional Lagrangian method is still used to calculate the deformation.

Figure 1 schematically outlines the step involved in the layer addition and removal mesh motion scheme:

- (a) The workpiece (e.g., wire) mesh is constructed such that it is layered in the streamwise direction.
- (b) Solution of the discretised governing equations provides the cell centres displacement increments  $\Delta\mathbf{u}$ .
- (c) The cell-centred displacement increment  $\Delta\mathbf{u}$  are interpolated to the vertices  $\Delta\mathbf{u}_v$ .
- (d) If the average width (in the streamwise direction) at the upstream boundary of the cell layer  $d_{av}$  is greater than a user-prescribed maximum width  $d_{max}$ , a zero-thickness layer of cells is added. The displacement increments of the newly added layer of vertices are taken from the upstream boundary vertices.
- (e) The vertex displacement increments  $\Delta\mathbf{u}_v$  at the upstream and downstream boundaries are set to zero, except for the newly added vertices, which form part of the zero-thickness layer.
- (f) The mesh is moved by the vertex displacement increment field  $\Delta\mathbf{u}_v$ , where it is noted that the vertices on the upstream and downstream points do not move; this causes the newly added cell layer to *grow* by the displacement increment field.
- (g) If the average width (in the streamwise direction) of the cell layer  $d_{av}$  at the downstream boundary is less than a user-prescribed minimum width  $d_{min}$ , remove the layer of cells at the downstream boundary. Depending on displacement increment magnitude, multiple cell layers may need to be iteratively removed.

Following the layer addition and removal mesh motion algorithm, solution and derived field data at the newly added cell centres are mapped from the field data stored at the upstream boundary. This mapping approach assumes field data to have a zero gradient in the upstream direction; this assumption is valid if the upstream and downstream are chosen sufficiently far from the *active* deformation zone.

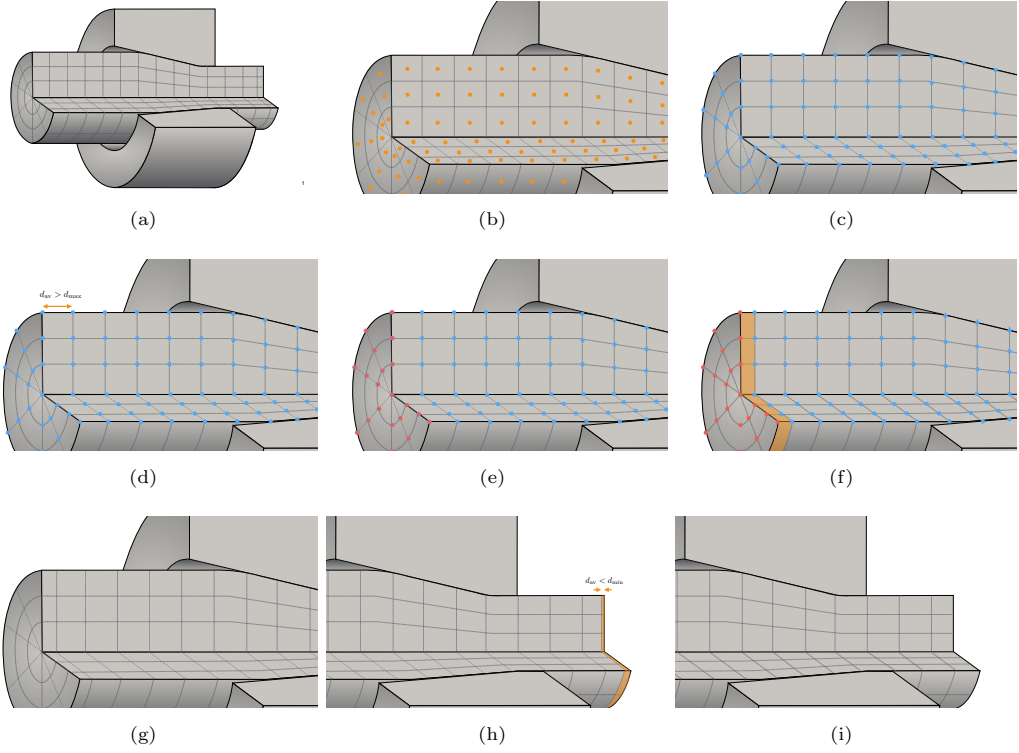


**Fig. 1** Layer addition and removal mesh motion algorithm for continuous wire drawing (a). The displacement increments are calculated at the cell centre (b) and are interpolated to the vertices (c). A new layer of cells is added at the upstream boundary if the layer width is greater than  $d_{\max}$  (d-g). Layers of cells are removed from the downstream boundary if the later width is less than  $d_{\max}$  (h-i).

**Note on parallelisation:** The proposed solution algorithm has been implemented in the open-source toolbox OpenFOAM, where multi-CPU-core parallelisation on distributed memory systems is achieved through the domain decomposition approach. To simplify the implementation of the non-trivial topological mesh changes (addition or removal of cells) in parallel, domain decomposition approaches are limited to decomposing the workpiece into streamwise columns of cells (Figure 2). In the current approach, modified forms of the METIS [48] and scotch [49] approaches have been used to perform this decomposition. Nonetheless, there is no limitation on the decomposition of the cells in the die, as demonstrated in Figure 2.

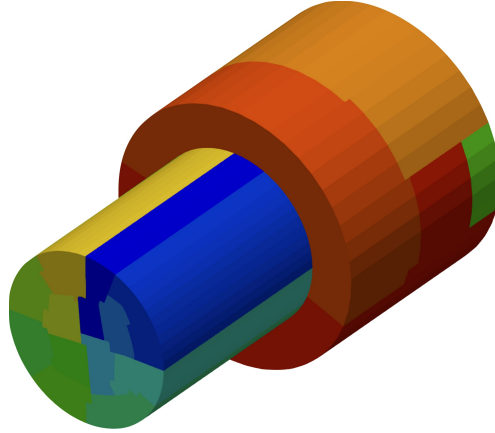


**Fig. 2** Example parallel decomposition of a wire and drawing die, where the wire is decomposed into streamwise columns, indicated by the different colours. There is no limitation on the die decomposition.

### 3 Constitutive damage laws

#### 3.1 Overview

As noted by Garrison and Moody [50], ductile fracture in metals occurs in three stages: (i) voids are nucleated at material defects (usually inclusions), adding to pre-existing voids, if any; (ii) plastic deformations cause these voids to grow; and (iii) when large enough, these voids coalesce to form micro-cracks and macro-cracks. As noted in the introduction, approaches for modelling ductile fracture in metal forming can be classified into two approaches [9, 10]: continuum damage mechanics models and micro-mechanical models.

In *continuum* damage mechanics, an internal damage variable is used to describe the accumulation of microstructural degradation within a material due to various types of loading. This degradation is typically reflected in the increased density of internal defects, such as microcracks, dislocations, or voids. The internal damage variable is continuous, meaning it can take on any value within a given range. The *micro-mechanical* approach is also continuous in nature and posits the existence of material micro-voids. The void density is described by a *porosity* variable. Material degradation is characterised by increased porosity due to void nucleation, growth, and coalescence. As noted by Besson [14], Cao [9] and Tekkaya et al. [10], the canonical frameworks in the continuum damage mechanics and micro-mechanical approaches are the Lemaitre [19, 20] and the Gurson-Tvergaard-Needleman (GTN) [21, 22] models, respectively.

This section provides an overview of the classic Lemaitre and GTN models and proposes modifications to the Lemaitre model to extend its applicability to high hydrostatic pressure regimes characteristic of wire drawing. For comparison, a recent phase field model damage approach is also considered.

The constitutive damage laws described in this section close the system of governing equations (Equation 4) described in Section 2.2 by providing the true stress definition.

#### 3.2 Preliminaries

Before describing these models in more detail, it is necessary to define the stress triaxiality  $\eta$ , the Lode angle  $\theta$  and related Lode parameters [51, 52]. Extensive literature has noted the importance of stress triaxiality and Lode angle in predicting ductile fracture [9, 10, 14]. The triaxiality parameter  $\eta$  is given by:

$$\eta = -\frac{p}{\sigma_v} \quad (18)$$

where, as noted previously,  $p = -\text{tr}(\boldsymbol{\sigma})/3$  is the hydrostatic pressure, and  $\sigma_v = \sqrt{3J_2} = \sqrt{\frac{3}{2}\text{dev}(\boldsymbol{\sigma}):\text{dev}(\boldsymbol{\sigma})}$  is the equivalent (von Mises) stress.  $J_2$  is the second invariant of the deviatoric stress tensor. The deviatoric operator is indicated by  $\text{dev}(\bullet)$ , and  $:$  indicates the double-dot product.

The Lode angle,  $0 \leq \theta \leq \frac{\pi}{3}$ , can be physically interpreted as the degree of shear dominance in the stress state. The Lode angle can be rewritten as a function of the normalised third invariant

of the deviatoric stress tensor:

$$\theta = \frac{1}{3} \arccos(\xi) \quad (19)$$

The parameter  $0 \leq \xi \leq 1$  is determined as a ratio between the third invariant and the equivalent stress:

$$\xi = \left( \frac{r}{\sigma_v} \right)^3 \quad (20)$$

where  $r$  is given by:

$$r = 3 \left( \frac{3}{2} J_3 \right)^{1/3} \quad (21)$$

The third invariant of the deviatoric stress tensor is  $J_3 = \det[\text{dev}(\boldsymbol{s})]$ . An alternative normalised Lode angle has been proposed by Bai and Wierzbicki [51] to be

$$\bar{\theta} = 1 - \frac{6\theta}{\pi} \quad (22)$$

which ranges between -1 and 1.

The three Lode parameters ( $\theta$ ,  $\xi$ , and  $\bar{\theta}$ ) are essentially equivalent but are defined to vary between different limits.

### 3.3 Isotropic Elastoplasticity

#### 3.3.1 Model Formulation

In the current work, the damage models are formulated in terms of isotropic  $J_2$  (von Mises) elastoplasticity. Extension to other forms of elastoplasticity (e.g., kinematic hardening, anisotropic/Hill yielding, distortional hardening) is possible but is outside the scope of this article. The adopted large strain elastoplasticity formulation is based on the logarithmic (Hencky) strain, as proposed by Eterovic and Bathe [53] and described in detail by Koji and Bathe [54] and de Souza Neto et al. [55]. This approach allows an additive split of the elastic and plastic strain tensors, conveniently leading to a return mapping scheme that is similar in form to those used in small-strain deformation models. In contrast, previous large-strain elastoplastic models [11, 13] implemented in the OpenFOAM software have adopted the approaches of Caminero et al. [56] and Simo and Hughes [57].

The employed isotropic  $J_2$  elastoplastic constitutive law is defined in terms of the yield criterion

$$\Phi = \sigma_v - \sigma_y(\bar{\varepsilon}_p) \quad (23)$$

and flow rule

$$\dot{\mathbf{F}}_p \mathbf{F}_p^{-1} = \dot{\varepsilon}_p \mathbf{R}_e^T \left[ \frac{3}{2} \frac{\text{dev}(\boldsymbol{\sigma})}{\sigma_v} \right] \mathbf{R}_e \quad (24)$$

where the yield stress  $\sigma_y$  is a function of the hardening variable  $\bar{\varepsilon}_p$ , which coincides with the equivalent plastic strain  $\bar{\varepsilon}_p$ . The deformation gradient is decomposed into elastic and plastic components

$\mathbf{F} = \mathbf{F}_e \mathbf{F}_p$  and polar decomposition of the elastic deformation gradient gives the elastic rotation  $\mathbf{R}_e$  and elastic stretch  $\mathbf{U}_e$  tensors:  $\mathbf{F}_e = \mathbf{R}_e \mathbf{U}_p$ .

The model is closed with the Kuhn-Tucker conditions

$$\Phi \geq 0, \quad \dot{\bar{\varepsilon}}_p \geq 0, \quad \dot{\bar{\varepsilon}}_p \Phi = 0 \quad (25)$$

and the consistency condition

$$\dot{\bar{\varepsilon}}_p \dot{\Phi} = 0 \quad (26)$$

### 3.3.2 Computational procedure

For each cell at every outer (Picard) iteration, the stress  $\boldsymbol{\sigma}^{[m+1]}$  and history variables  $(\alpha^{[m+1]}, \mathbf{F}_p^{[m+1]})$  at time step  $t^{[m+1]}$  must be calculated in terms of the current displacement increment gradient  $[\nabla(\Delta\mathbf{u})]^{[m+1]}$  and old-time history variables  $(\alpha^{[m]}, \mathbf{F}_p^{[m]})$ .

The adopted stress calculation algorithm [55] is summarised in Algorithm 2.

## 3.4 Lemaitre Damage Model

### 3.4.1 Model Formulation

The Lemaitre model describes damage using a scalar field variable  $D$ . When no damage has occurred, the damage variable  $D$  equals 0 (virgin material), whereas when the material is fully damaged, the damage variable equals 1. From a physical point of view,  $D$  can be interpreted as the area of cracks and cavities per unit surface cut by an arbitrary plane.

The Lemaitre model augments the elastoplasticity constitutive law (Equations 23 and 24) with the inclusion of an evolution law for  $D$ . In addition, the reciprocal of  $(1 - D)$  is introduced to the yield function and flow rules:

$$\Phi = \frac{\sigma_v}{1 - D} - \sigma_y(\bar{\varepsilon}_p) \quad (27)$$

$$\dot{\mathbf{F}}_p \mathbf{F}_p^{-1} = \frac{\dot{\bar{\varepsilon}}_p}{1 - D} \mathbf{R}_e^T \left[ \frac{3}{2} \frac{\text{dev}(\boldsymbol{\sigma})}{\sigma_v} \right] \mathbf{R}_e \quad (28)$$

$$\dot{D} = \frac{\dot{\bar{\varepsilon}}_p}{1 - D} \left( \frac{-Y}{S_0} \right)^b \quad (29)$$

where  $S_0$  (dimensions of stress) and  $b$  (dimensionless) are material parameters. The energy release rate  $Y$ , which gives the energy dissipated due to the phenomenon of damage, is given by [20]

$$Y = -\frac{\sigma_v^2}{2E} \left[ \frac{2}{3}(1 + \nu) + 3(1 - 2\nu)\eta^2 \right] \quad (30)$$

---

**Algorithm 2:** Large strain  $J_2$  (von Mises) isotropic elastoplastic stress calculation algorithm [55]

---

(i) Update deformation gradients for a given incremental displacement

$$\mathbf{f}^{[m+1]} = \mathbf{I} + [\nabla(\Delta\mathbf{u})]^T$$

$$\mathbf{F}^{[m+1]} = \mathbf{f}^{[m+1]} \mathbf{F}^{[m]}$$

$$J^{[m+1]} = \det(\mathbf{F}^{[m+1]})$$

(ii) Compute trial elastic state

$$\mathbf{B}_e^{[m]} = \exp(2\boldsymbol{\epsilon}_e^{[m]})$$

$$\mathbf{B}_e^{\text{trial}} = \mathbf{f}^{[m+1]} \mathbf{B}_e^{[m]} (\mathbf{f}^{[m+1]})^T$$

$$\boldsymbol{\epsilon}_e^{\text{trial}} = \frac{1}{2} \ln(\mathbf{B}_e^{\text{trial}})$$

$$\bar{\boldsymbol{\epsilon}}_p^{\text{trial}} = \bar{\boldsymbol{\epsilon}}_p^{[m]}$$

$$\sigma_v^{\text{trial}} = \sqrt{3/2} ||2\mu \text{dev}(\boldsymbol{\epsilon}_e^{\text{trial}})||$$

$$\Phi^{\text{trial}} = \sigma_v^{\text{trial}} - \sigma_y(\bar{\boldsymbol{\epsilon}}_p^{\text{trial}})$$

**if**  $\Phi^{\text{trial}} > 0$  **then**

| Go to step (iii) to solve for  $\Delta\bar{\boldsymbol{\epsilon}}_p$

**else**

|  $\Delta\bar{\boldsymbol{\epsilon}}_p = 0$  and go to step (iv)

**end**

(iii) Use the Newton-Raphson method to solve the yield function for  $\Delta\bar{\boldsymbol{\epsilon}}_p$ :

$$\sigma_v^{\text{trial}} - 3\mu\Delta\bar{\boldsymbol{\epsilon}}_p - \sigma_y(\bar{\boldsymbol{\epsilon}}_p^{[m]} + \Delta\bar{\boldsymbol{\epsilon}}_p) = 0$$

(iv) Update the constitutive variables and deviatoric stress

$$\boldsymbol{\epsilon}_e^{[m+1]} = \boldsymbol{\epsilon}_e^{\text{trial}} - \sqrt{3/2} \Delta\bar{\boldsymbol{\epsilon}}_p \frac{\text{dev}(\boldsymbol{\epsilon}_e^{\text{trial}})}{||\boldsymbol{\epsilon}_e^{\text{trial}}||}$$

$$\bar{\boldsymbol{\epsilon}}_p^{[m+1]} = \bar{\boldsymbol{\epsilon}}_p^{[m]} + \Delta\bar{\boldsymbol{\epsilon}}_p$$

$$\hat{p} = -\frac{\kappa}{J^{[m+1]}} \text{tr}(\boldsymbol{\epsilon}_e^{[m+1]})$$

$$\mathbf{s}^{[m+1]} = (1/J^{[m+1]}) 2\mu \text{dev}(\boldsymbol{\epsilon}_e^{[m+1]})$$

(v) **if** Solve pressure equation **then**

Implicitly solve the pressure Poisson's equation:

$$p^{[m+1]} - \mathbb{D}\nabla^2 p^{[m+1]} = \hat{p} - \nabla \cdot (\mathbb{D}\nabla p_{[i]}^{[m+1]})$$

**else**

**end**

(vi) Update the true (Cauchy) stress

$$\boldsymbol{\sigma}^{[m+1]} = \mathbf{s}^{[m+1]} - p^{[m+1]} \mathbf{I}$$


---

where  $E$  is Young's modulus and  $\nu$  is Poisson's ratio, and the dependence on  $Y$  on triaxiality ( $\eta = p/\sigma_v$ ) is explicitly clear.

### Triaxiality and Lode Angle Dependence

The classic Lemaitre model does not distinguish between positive and negative triaxiality ( $\eta$  is squared in Equation 30); consequently, it can overpredict damage in wire drawing processes where triaxiality can be highly negative (high negative/tensile pressures). One remedy is to employ a triaxiality cut-off [58], which disallows damage evolution for highly negative triaxiality values:

$$\dot{D} = \begin{cases} 0 & \text{if } \eta \leq -\frac{1}{3} \\ \frac{\dot{\bar{\boldsymbol{\epsilon}}}_p}{1-D} \left( \frac{-Y}{S_0} \right)^b & \text{if } \eta > -\frac{1}{3} \end{cases} \quad (31)$$

Rather than use a triaxiality cut-off, Malcher and co-workers [59–61] proposed that the parameter  $S_0$  be a function of triaxiality  $\eta$  as well as Lode angle  $\xi$ . This approach has shown an ability to accurately predict fracture for a range of loading conditions at both low and high triaxiality values and for various shear stress states. The Malcher et al. form of damage evolution is achieved by making  $S_0$  in Equation 29 a function of  $\eta$  and  $\xi$ :

$$S(\eta, \xi) = \frac{S_{0.33}}{3|\eta| + \frac{S_{0.33}}{S_{0.0}}(1 - \xi^2)} \quad (32)$$

where  $S_{0.33}$  and  $S_{0.0}$  are material parameters determined based on pure tensile loading ( $S_{0.33}$ ) and pure shear loading ( $S_{0.0}$ ).

Despite its success, this formulation's weakness is that it does not distinguish between positive and negative triaxiality values, which is critical for wire drawing. To overcome this limitation, a function for  $S(\eta, \xi)$  is proposed here, inspired by the Ko et al. [62] uncoupled damage law. The Ko et al. [62] criterion has shown an ability to predict fracture in both wire drawing processes [63] and in the hub-hole expanding process [62]. For the wire drawing,  $\xi \approx 1.0$  at the wire centre, where fracture originates [63]. For this reason, the proposed function does not incorporate a dependency on  $\xi$ , and the final expression for  $S$  proposed here takes the form

$$S(\eta) = \frac{2S_0}{1.0 + 3\eta} \quad (33)$$

### **Crack Closure Effects**

An additional limitation of the classic Lemaitre damage model is that it does not distinguish between tensile and compressive stress states, whereas it is known from experiments that tensile stresses are considerably more conducive to crack growth than compressive stresses [64]. To overcome this shortcoming, some authors assume no crack growth in compressive stress states [65]; however, this does not account for the partial closure of micro-defects under compressive stress states. This effect causes a greater material area to bear the compressive load. As a result, the material may exhibit a partial or complete recovery of its stiffness, depending on the specific conditions [66]. This approach also does not account for the fact that some crack growth can occur in compressive states [67].

Consequently, an *enhanced* Lemaitre model with crack closure effects has been proposed [66, 68]. In this approach, the energy release rate  $Y$  (Equation 30) is rewritten to account for the differing contributions of tensile and compressive stresses:

$$Y = \frac{-1}{2E(1-D)} [(1+\nu)\boldsymbol{\sigma}^+ : \boldsymbol{\sigma}^+ - \nu \langle \text{tr}(\boldsymbol{\sigma}) \rangle^2] - \frac{h}{2E(1-hD)} [(1+\nu)\boldsymbol{\sigma}^- : \boldsymbol{\sigma}^- - \nu \langle -\text{tr}(\boldsymbol{\sigma}) \rangle^2] \quad (34)$$

where Macaulay brackets are indicated by  $\langle \bullet \rangle$ . The parameter  $0 \leq h \leq 1$  accounts for the crack closure phenomenon; here, we take  $h = 0.2$  as is common for steels [58, 69, 70]). The positive and

negative stress components are defined as

$$\boldsymbol{\sigma}^+ = \sum_{i=1}^3 \langle \sigma_i \rangle \mathbf{e}_i \otimes \mathbf{e}_i \quad (35)$$

$$\boldsymbol{\sigma}^- = \sum_{i=1}^3 \langle -\sigma_i \rangle \mathbf{e}_i \otimes \mathbf{e}_i \quad (36)$$

where  $\sigma_i$  are the principal stresses,  $\{\mathbf{e}_1, \mathbf{e}_2, \mathbf{e}_3\}$  are the orthonormal basis vectors, and  $\boldsymbol{\sigma} = \boldsymbol{\sigma}^+ + \boldsymbol{\sigma}^-$ .

A simplified form of the crack-closure model [66] is employed in this work, whereby this definition of decomposed stress is only used in the damage evolution calculation.

### **Non-Local Damage**

One general limitation of damage models is that due to the strain softening behaviour, predictions may suffer from mesh size and orientation dependency in localised strain zones [71–73]. To rectify this, an implicit *non-local* damage variable  $\bar{D}$  is introduced as in Peerlings et al. [71, 72] and Geers et al. [73]. This is related to the local damage variable  $D$  through the implicit diffusion equation:

$$\bar{D} - l_c^2 \nabla^2 \bar{D} = D \quad (37)$$

where  $l_c$  is a characteristic length scale which controls the area over which the local damage is diffused. This equation can be viewed as a smoothing equation ( $\bar{D}$  is a spatially smoothed version of  $D$ ), which has the effect of mitigating the mesh dependency. This equation is solved with zero-flux Neumann boundary conditions on all boundaries, that is,  $\mathbf{n} \cdot \nabla \bar{D} = 0$ . The terms in Equation 37 are discretised using the cell-centred finite volume method, similar to the pressure equation (Equation 14).

#### **3.4.2 Computational Procedure**

An deferred (defect) algorithm is developed in this work to solve Equations 27-29. At every outer iteration, the plastic increment is solved implicitly, with the value for the damage variable fixed from the previous outer iteration. The damage rate equation (Equation 29) is then solved in a deferred-correction manner using the damage from the previous iteration,  $\bar{D}_{[i]}$ , where  $[i]$  indicates a value from a previous outer iteration. This approach avoids the use of a  $2 \times 2$  matrix (or an even higher dimension matrix if one were to solve for anisotropic plasticity or plasticity incorporating kinematic hardening) that would be needed if both the damage and the plastic increment were solved for implicitly simultaneously. By not requiring the solution of plasticity and damage simultaneously, the mathematics are simplified when solving for more complex formulations of the Lemaître damage evolution equation and the non-local damage. Note that the overall solution algorithm is still implicit in time.

This stress calculation procedure for the Lemaître damage model is summarised in Algorithm 3, where  $\bar{D}_{[i]}^{[m+1]}$  is the latest available non-local damage field at the new time, i.e. its values from

the previous outer iteration. Within each time step,  $\bar{D}_{[i]}^{[m+1]}$  converges to  $\bar{D}_{[i+1]}^{[m+1]}$ . As shown in Algorithm 3, to aid numerical convergence, a critical damage parameter  $D_c$  is incorporated [19], which limits the maximum value of the damage  $D$  to  $D_c$ , rather than 1. In the current work,  $D_c = 0.99$  is assumed. Consequently, the damage rate equation (Equation 30) becomes

$$\dot{D} = \begin{cases} 0 & \text{if } \eta \leq -\frac{1}{3} \text{ or } D \geq D_c \\ \frac{\dot{\varepsilon}_p}{1-D} \left( \frac{-Y}{S(\eta, \xi)} \right)^b & \text{if } \eta > -\frac{1}{3} \text{ and } D < D_c \end{cases} \quad (38)$$

where  $S$  can be a function of  $\eta$  and  $\xi$  as described above.

Although subtle, we have found that limiting the value of the non-local damage field  $\bar{D}$  (step (viii)) is critical for achieving reliable predictions. This step prevents nonphysical behaviour whereby a cell that is set as being fully damaged ( $D = D_c$ ) is contributing to the damage growth in the surrounding cells through the non-local damage field.

### 3.5 Gurson-Tvergaard-Needleman Model

#### 3.5.1 Model Formulation

Gurson [21] proposed the canonical micro-mechanical framework for ductile damage prediction and provided the basis for various derived models [9, 10, 14, 74, 75]. This model posits the existence of micro-voids in the material. The density of these voids is described by a variable denoted as porosity  $f$ . Material degradation is characterised by increasing porosity due to the growth of these voids. Gurson's framework was further developed by Tvergaard and Needleman [22] to account for the void nucleation and coalescence, leading to the Gurson-Tvergaard-Needleman (GTN) model.

The GTN model is described by a yield equation, flow rule (with deviatoric and volumetric components), consistency condition, and porosity evolution equations:

$$\Phi = \left( \frac{\sigma_v}{\sigma_y} \right)^2 + 2q_1 f_* \cosh \left( \frac{3q_2 p}{2\sigma_y} \right) - (1 + q_3 f_*^2) \quad (39)$$

$$\dot{\varepsilon}_p = \frac{1}{(1-f)\sigma_y} (\sigma_v \dot{\varepsilon}_{\text{dev}} - p \dot{\varepsilon}_{\text{vol}}) \quad (40)$$

$$\dot{\varepsilon}_{\text{vol}} \frac{\partial \Phi}{\partial \sigma_v} + \dot{\varepsilon}_{\text{dev}} \frac{\partial \Phi}{\partial p} = 0 \quad (41)$$

$$\dot{f} = (1 - f) \text{tr}(\dot{\varepsilon}_p) + A \dot{\varepsilon}_p \quad (42)$$

where  $q_1$ ,  $q_2$  and  $q_3$  are dimensionless material parameters. The effective void fraction  $f_*$ , which accounts for void coalescence, is

$$f_* = \begin{cases} f & \text{if } f \leq f_c \\ f_c + (f - f_c) \frac{f_u - f_c}{f_f - f_c} & \text{if } f > f_c \end{cases} \quad (43)$$

where  $f_c$  is the void volume fraction at which void coalescence begins,  $f_u$  is the ultimate volume fraction, and  $f_f$  is the void volume fraction at fracture.

---

**Algorithm 3:** Lemaitre damage model stress calculation algorithm

---

(i) Update deformation gradients for a given incremental displacement

$$\begin{aligned}\mathbf{f}^{[m+1]} &= \mathbf{I} + [\nabla(\Delta\mathbf{u})]^T \\ \mathbf{F}^{[m+1]} &= \mathbf{f}^{[m+1]} \mathbf{F}^{[m]} \\ J^{[m+1]} &= \det(\mathbf{F}^{[m+1]})\end{aligned}$$

(ii) Compute trial elastic state

$$\begin{aligned}\mathbf{B}_e^{[m]} &= \exp(2\boldsymbol{\epsilon}_e^{[m]}) \\ \mathbf{B}_e^{\text{trial}} &= \mathbf{f}^{[m+1]} \mathbf{B}_e^{[m]} (\mathbf{f}^{[m+1]})^T \\ \boldsymbol{\epsilon}_e^{\text{trial}} &= \frac{1}{2} \ln(\mathbf{B}_e^{\text{trial}}) \\ \bar{\boldsymbol{\epsilon}}_p^{\text{trial}} &= \bar{\boldsymbol{\epsilon}}_p^{[m]} \\ \sigma_v^{\text{trial}} &= \sqrt{3/2} \|2G \operatorname{dev}(\boldsymbol{\epsilon}_e^{\text{trial}})\| \\ \Phi^{\text{trial}} &= \sigma_v^{\text{trial}} - \sigma_y(\bar{\boldsymbol{\epsilon}}_p^{\text{trial}})\end{aligned}$$

```

if  $\Phi^{\text{trial}} > 0$  then
    | Go to step (iii) to solve for  $\Delta\bar{\boldsymbol{\epsilon}}_p$ 
else
    |  $\Delta\bar{\boldsymbol{\epsilon}}_p = 0$  and go to step (iv)
end

```

(iii) Use the Newton-Raphson method to solve the yield function for  $\Delta\bar{\boldsymbol{\epsilon}}_p$ :

$$\sigma_v^{\text{trial}} - \frac{3\mu\Delta\bar{\boldsymbol{\epsilon}}_p}{1 - \bar{D}_{[i]}^{[m+1]}} - \sigma_y(\bar{\boldsymbol{\epsilon}}_p^{[m]} + \Delta\bar{\boldsymbol{\epsilon}}_p) = 0$$

(iv) Update constitutive variables and deviatoric stress

$$\begin{aligned}\boldsymbol{\epsilon}_e^{[m+1]} &= \boldsymbol{\epsilon}_e^{\text{trial}} - \sqrt{\frac{3}{2}} \frac{\Delta\bar{\boldsymbol{\epsilon}}_p}{1 - \bar{D}_{[i]}^{[m+1]}} \frac{\operatorname{dev}(\boldsymbol{\epsilon}_e^{\text{trial}})}{\|\boldsymbol{\epsilon}_e^{\text{trial}}\|} \\ \bar{\boldsymbol{\epsilon}}_p^{[m+1]} &= \bar{\boldsymbol{\epsilon}}_p^{[m]} + \Delta\bar{\boldsymbol{\epsilon}}_p \\ \hat{p} &= -\left(1 - \bar{D}_{[i]}^{[m+1]}\right) \frac{\kappa}{J^{[m+1]}} \operatorname{tr}(\boldsymbol{\epsilon}_e^{[m+1]}) \\ \mathbf{s}^{[m+1]} &= \left(1 - \bar{D}_{[i]}^{[m+1]}\right)^{(1/J)} 2\mu \operatorname{dev}(\boldsymbol{\epsilon}_e^{[m+1]})\end{aligned}$$

(v) if Solve pressure equation then

```

Implicitly solve the pressure Poisson's equation:

$$p^{[m+1]} - \mathbb{D}\nabla^2 p^{[m+1]} = \hat{p} - \nabla \cdot (\mathbb{D}\nabla p_{[i]}^{[m+1]})$$

else
    
$$p^{[m+1]} = \hat{p}$$

end

```

(vi) Update the true (Cauchy) stress

$$\boldsymbol{\sigma}^{[m+1]} = \mathbf{s}^{[m+1]} - p^{[m+1]} \mathbf{I}$$

(vii) Update the local damage (use the modified form for  $Y$  if the crack  $h > 0$ )

$$D^{[m+1]} = \begin{cases} D^{[m]} & \text{if } \eta \leq -\frac{1}{3} \text{ or } D_{[i]}^{[m+1]} \geq D_c \\ \max \left[ D^{[m]} + \frac{\dot{\bar{\boldsymbol{\epsilon}}}_p}{1 - \bar{D}_{[i]}^{[m+1]}} \left( \frac{-Y}{S(\eta, \xi)} \right)^b, D_c \right] & \text{if } \eta > -\frac{1}{3} \text{ and } D_{[i]}^{[m+1]} < D_c \end{cases}$$

(viii) Implicitly solve diffusion equation for non-local damage

$$\bar{D}^{[m+1]} - l_c^2 \nabla^2 \bar{D}^{[m+1]} = D^{[m+1]}$$

(ix) Limit the non-local damage

$$\bar{D}^{[m+1]} = \max(\bar{D}^{[m+1]}, D_c)$$


---

The rate of volumetric plastic strain and equivalent deviatoric plastic strain are given, respectively, by

$$\dot{\epsilon}_{\text{vol}} = -\dot{\bar{\boldsymbol{\epsilon}}}_p \frac{\partial \Phi}{\partial p} \quad (44)$$

$$\dot{\epsilon}_{\text{dev}} = \dot{\bar{\boldsymbol{\epsilon}}}_p \frac{\partial \Phi}{\partial \sigma_v} \quad (45)$$

The dimensionless coefficient  $A$  is chosen to ensure void nucleation follows a normal distribution [65]:

$$A = \begin{cases} \frac{f_n}{S_n \sqrt{2\pi}} \exp\left[-\frac{1}{2}\left(\frac{\bar{\varepsilon}_p - \varepsilon_n}{S_n}\right)\right] & \text{if } p < 0 \\ 0 & \text{if } p \geq 0 \end{cases} \quad (46)$$

where  $f_n$  determines the total void fraction possible,  $\varepsilon_n$  is the mean nucleation strain, and  $S_n$  is the nucleation strain standard deviation.

### **Lode Angle Dependence**

Further developments of the GTN model have been made to better account for fracture in stress states with significant shearing [52, 75–77]. This work adopts the expression developed by Nahshon and Hutchinson [52] for shearing-related void growth, which has shown an ability to accurately predict fracture in the blanking metal forming process [75]. The porosity evolution equation (Equation 42) is consequently replaced by

$$\dot{f} = (1 - f) \operatorname{tr}(\dot{\varepsilon}_p) + A \dot{\bar{\varepsilon}}_p + k_w f \frac{1 - \xi^2}{\sigma_v} \operatorname{dev}(\boldsymbol{\sigma}) : \dot{\varepsilon}_p \quad (47)$$

where  $k_w$  is a material parameter.

### **Non-Local Porosity**

Like the Lemaitre model, mesh dependency in the GTN model can be mitigated by introducing non-local damage variables [77, 78]. In the case of the GTN model, a non-local (smoothed) porosity variable  $\bar{f}$  is determined using a non-local gradient (smoothing) equation:

$$\bar{f} - l_c^2 \nabla^2 \bar{f} = f \quad (48)$$

As before, this equation can be discretised using the described cell-centred finite volume method and zero-flux Neumann boundary conditions.

### **3.5.2 Computational Procedure**

For the GTN model, the elastoplasticity stress calculation is extended to determine porosity  $f$  in addition to stress and plastic strain. The adopted computational algorithm is shown in Algorithm 4. As in the Lemaitre computational procedure, we propose a deferred correction algorithm to solve the system of equations: Equations 39, 40 and 41 are solved implicitly for the variables  $\varepsilon_{\text{vol}}$ ,  $\varepsilon_{\text{dev}}$  and  $\bar{\varepsilon}_p$  using a Newton-Raphson method, while the porosity  $f$  (Equation 42) is calculated in a deferred-correction/explicit manner. Once again, the overall procedure is implicit in time.

---

**Algorithm 4:** GTN damage model stress calculation algorithm

---

(i) Update deformation gradients for a given incremental displacement

$$\begin{aligned}\mathbf{f}^{[m+1]} &= \mathbf{I} + [\nabla(\Delta\mathbf{u})]^T \\ \mathbf{F}^{[m+1]} &= \mathbf{f}^{[m+1]} \mathbf{F}^{[m]} \\ J^{[m+1]} &= \det(\mathbf{F}^{[m+1]})\end{aligned}$$

(ii) Compute trial elastic state

$$\begin{aligned}\mathbf{B}_e^{[m]} &= \exp(2\boldsymbol{\epsilon}_e^{[m]}) \\ \mathbf{B}_e^{\text{trial}} &= \mathbf{f}^{[m+1]} \mathbf{B}_e^{[m]} (\mathbf{f}^{[m+1]})^T \\ \boldsymbol{\epsilon}_e^{\text{trial}} &= \frac{1}{2} \ln [\mathbf{B}_e^{\text{trial}}] \\ p^{\text{trial}} &= -\kappa \operatorname{tr}(\boldsymbol{\epsilon}_e^{\text{trial}}) \\ \mathbf{s}^{\text{trial}} &= 2\mu \operatorname{dev}(\boldsymbol{\epsilon}_e^{\text{trial}}) \\ \sigma_v^{\text{trial}} &= \sqrt{3/2} ||2\mu \operatorname{dev}(\boldsymbol{\epsilon}_e^{\text{trial}})|| \\ \mathbf{n} &= \frac{3}{2} \frac{\mathbf{s}^{\text{trial}}}{\sigma_v^{\text{trial}}} \\ \Phi^{\text{trial}} &= \left( \frac{\sigma_v^{\text{trial}}}{\sigma_y} \right)^2 + q_1 f_{*[i]}^{[m+1]} \cosh \left( \frac{3q_2 p^{\text{trial}}}{2\sigma_y} \right) - (1 + q_3 f_{*[i]}^{[m+1]2})\end{aligned}$$

```

if  $\Phi^{\text{trial}} > 0$  then
| Go to step (iii)
else
| set  $\Delta\boldsymbol{\epsilon}_{\text{vol}} = \Delta\boldsymbol{\epsilon}_{\text{dev}} = \Delta\bar{\boldsymbol{\epsilon}}_p = 0$  and  $\Delta\boldsymbol{\epsilon}_p = \mathbf{0}$ . Go to step (iv)
end

```

(iii) Enter small strain return map and solve the system of equations (Equations 49-51) for  $\Delta\boldsymbol{\epsilon}_h^{[m+1]}$ ,  $\Delta\boldsymbol{\epsilon}_q^{[m+1]}$  and  $\Delta\bar{\boldsymbol{\epsilon}}_{[m+1]}^p$

(iv) Update the constitutive variables

$$\begin{aligned}\bar{\boldsymbol{\epsilon}}_p^{[m+1]} &= \boldsymbol{\epsilon}_p^{[m]} + \Delta\bar{\boldsymbol{\epsilon}}_p \\ \boldsymbol{\epsilon}_p^{[m+1]} &= \boldsymbol{\epsilon}_p^{[m]} + \Delta\boldsymbol{\epsilon}_p \\ \boldsymbol{\epsilon}_e^{[m+1]} &= \boldsymbol{\epsilon}^{\text{trial}} - (1/3)\Delta\boldsymbol{\epsilon}_{\text{vol}}^{[m+1]} \mathbf{I} - \Delta\boldsymbol{\epsilon}_{\text{dev}}^{[m+1]} \mathbf{n} \\ \hat{p} &= p^{\text{trial}} + \kappa\Delta\boldsymbol{\epsilon}_{\text{vol}}^{[m+1]} \\ \mathbf{s}^{[m+1]} &= \frac{1}{J} [2/3 (\sigma_v^{\text{trial}} - 3\mu\Delta\boldsymbol{\epsilon}_{\text{dev}}^{[m+1]}) \mathbf{n}]\end{aligned}\tag{49}$$

(v) if *Solve pressure equation* then

Implicitly solve the pressure Poisson's equation:

$$p^{[m+1]} - \mathbb{D}\nabla^2 p^{[m+1]} = \hat{p} - \nabla \cdot (\mathbb{D}\nabla p_{[i]}^{[m+1]})\tag{50}$$

else

$$p^{[m+1]} = \hat{p}\tag{51}$$

end

(vi) Update the true (Cauchy) stress

$$\boldsymbol{\sigma}^{[m+1]} = \mathbf{s}^{[m+1]} - p^{[m+1]} \mathbf{I}$$

(vii) Calculate the porosity  $f_{[i+1]}^{[m+1]}$  and the effective porosity  $f_{*[i+1]}^{[m+1]}$ :

$$f^{[m+1]} = f^{[m]} + \left(1 - f_{[i]}^{[m+1]}\right) \operatorname{tr}(\dot{\boldsymbol{\epsilon}}_p^{[m+1]}) + A\dot{\bar{\boldsymbol{\epsilon}}}_p^{[m+1]} + k_w f \frac{1 - \xi^2}{\sigma_v^{[m+1]}} \operatorname{dev}(\boldsymbol{\sigma}^{[m+1]}) : \dot{\boldsymbol{\epsilon}}_p^{[m+1]}\tag{52}$$

$$f^{*[m+1]} = \begin{cases} f^{[m+1]} & \text{if } f^{[m+1]} \leq f_c \\ f_c + \left(f^{[m+1]} - f_c\right) \frac{f_u - f_c}{f_f - f_c} & \text{if } f^{[m+1]} > f_c \end{cases}\tag{53}$$

(viii) Implicitly solve non-local porosity equation:

$$\bar{f}^{[m+1]} - l_c^2 \nabla^2 \bar{f}^{[m+1]} = f^{[m+1]}\tag{54}$$


---

## 3.6 Phase field fracture model

### 3.6.1 Model Formulation

In recent years, phase field approaches have received much attention for the prediction of fracture and failure [23–27, 79, 80], showing an ability to predict complex crack patterns, including

branching and merging in both two and three dimensions [79, 80]. In this method, sharp cracks are *regularised* over a continuum, leading to a system of partial differential equations that are relatively simple to implement in finite element, finite volume and related solvers.

The phase field method for damage, initially proposed by Francfort and Marigo [81] to describe brittle fracture, is based on a variational approach to minimise a Griffiths theory potential energy functional. This approach leads to a Mumford-Shah [82] type energy potential that can be approximated by a phase-field formulation following the work of Ambrosio and Tortorelli [83]. This approximation was adopted by Bourdin et al. [84] to facilitate numerical solutions of the variational formulation and further extended by Miehe et al. [80], who derived the phase field approach from continuum mechanics and thermodynamic arguments. Miehe et al. [80] also added an important mechanism for distinguishing between tensile and compressive effects on crack growth, as well as including a history variable  $\mathcal{H}$ , ensuring the irreversibility of crack growth. Several studies have shown the ability of these models to produce results consistent with benchmark fracture cases [79, 80].

The phase field approach has since been extended to ductile fracture by Ambati et al. [23], Borden et al. [24] and Miehe et al. [25]. The approach from Ambati et al. [23] involves incorporating a plastic strain dependency in the elastic degradation function while the approach from Miehe et al. [25] incorporates the plastic strain energy into the crack driving variable  $\mathcal{H}$ . Borden et al. [24] uses a similar approach to Miehe et al. [25] by incorporating the plastic strain into the crack driving variable  $\mathcal{H}$  while also introducing a plastic degradation function to ensure that fracture is preceded by large plastic strains, as is seen experimentally.

In this work, the approach from Borden et al. [24] is chosen to be most suitable, given the large plastic strains expected in wire drawing. The strong differential form of the phase field equation is given by:

$$\frac{G_c}{2l} (d - 4l^2 \nabla^2 d) = \mathcal{H} \quad (55)$$

where  $0 < d \leq 1$  is the damage variable, with  $d = 0$  characterising the unbroken state and  $d = 1$  characterising the fully broken state. The variable  $d$  is conceptually similar to the damage variable  $D$  used in the Lemaitre model and the porosity  $f$  in the GTN model, with  $d$  being a macroscopic variable that characterises the growth of micro-voids and micro-cracks. The critical fracture energy per unit area is given by  $G_c$ . The parameter  $l$  is a length-scale variable that regularises the crack surface. It is typically chosen as a function of the local element/cell size. The crack driving variable  $\mathcal{H}$  is

$$\mathcal{H} = -2d \max [\psi_e(\boldsymbol{\varepsilon}^e), \bar{\psi}_e(\boldsymbol{\varepsilon}^e)] - 2d\langle\psi_p(\bar{\boldsymbol{\varepsilon}}^p) - w_0\rangle \quad (56)$$

where  $\psi_e(\boldsymbol{\varepsilon}^e)$  is the current elastic energy contribution, and  $\bar{\psi}_e(\boldsymbol{\varepsilon}^e)$  is a history variable which gives the largest value reached by the elastic energy contribution in time. The elastic energy contribution  $\psi_e(\boldsymbol{\varepsilon}^e)$  is decomposed into positive and negative components, such that only positive elastic strain energy contributes towards the crack driving energy [85]:

$$\psi_e = (1 - d^2) \psi_e^+(\boldsymbol{\varepsilon}_e) + \psi_e^-(\boldsymbol{\varepsilon}_e) \quad (57)$$

$$\psi_e^+(\boldsymbol{\varepsilon}^e) = \frac{\kappa}{2} \langle \text{tr}(\boldsymbol{\varepsilon}_e) \rangle^2 + \mu \text{dev}(\boldsymbol{\varepsilon}_e) : \text{dev}(\boldsymbol{\varepsilon}_e) \quad (58)$$

$$\psi_e^-(\boldsymbol{\varepsilon}_e) = \frac{\kappa}{2} \langle -\text{tr}(\boldsymbol{\varepsilon}_e) \rangle^2 \quad (59)$$

The plastic energy contribution to the crack growth  $\psi_p(\bar{\varepsilon}^p)$  is given by [86]:

$$\psi_p(\bar{\varepsilon}^p) = \int_0^{\bar{\varepsilon}^p} \sigma_y d\bar{\varepsilon}^p \quad (60)$$

and  $w_0$  is the plastic work threshold, below which the plastic strain will not contribute to crack growth.

Finally, the isotropic  $J_2$  yield function (Equation 23) is modified as [24]

$$\Phi = \sigma'_v - (1 - d^2) \sigma_y (\bar{\varepsilon}_p) \quad (61)$$

where

$$\sigma'_v = \sqrt{3/2 \mathbf{s}' : \mathbf{s}'} \quad (62)$$

$$\mathbf{s}' = (1 - d^2) 2\mu \operatorname{dev}(\boldsymbol{\varepsilon}_e) \quad (63)$$

Similar to the non-local equations in the Lemaître and GTN models, in this work, the phase field equation (Equation 55) is discretised using the described cell-centred finite volume method, and zero-flux Neumann boundary conditions.

### 3.6.2 Computational Procedure

Similar to the Lemaître and GTN procedures, a deferred-correction procedure is adopted here to incorporate the phase (damage) evolution equation. Within each outer iteration, the elastoplastic quantities are calculated using the latest available phase field variable  $d_{(i)}^{[m+1]}$  from the previous outer iteration  $i$ . Subsequently, the phase field equation (Equation 55) is solved using the latest available stress and strain fields. The algorithm for the phase field stress calculation procedure is given in Algorithm 5.

---

**Algorithm 5:** Phase field damage model stress calculation algorithm

---

(i) Update deformation gradients for a given incremental displacement

$$\begin{aligned}\mathbf{f}^{[m+1]} &= \mathbf{I} + [\nabla(\Delta\mathbf{u})]^T \\ \mathbf{F}^{[m+1]} &= \mathbf{f}^{[m+1]} \mathbf{F}^{[m]} \\ J^{[m+1]} &= \det(\mathbf{F}^{[m+1]})\end{aligned}$$

(ii) Compute trial elastic state

$$\begin{aligned}\mathbf{B}_e^{[m]} &= \exp(2\boldsymbol{\varepsilon}_e^{[m]}) \\ \mathbf{B}_e^{\text{trial}} &= \mathbf{f}^{[m+1]} \mathbf{B}_e^{[m]} (\mathbf{f}^{[m+1]})^T \\ \boldsymbol{\varepsilon}_e^{\text{trial}} &= \frac{1}{2} \ln(\mathbf{B}_e^{\text{trial}}) \\ \sigma_v^{\text{trial}} &= (1 - d_{[i]}^{[m+1]2}) \sqrt{3/2} ||2\mu \text{dev}(\boldsymbol{\varepsilon}_e)|| \\ \Phi^{\text{trial}} &= \sigma_v^{\text{trial}} - (1 - d_{[i]}^{[m+1]2}) \sigma_y(\bar{\varepsilon}_p^{[m]})\end{aligned}$$

**if**  $\Phi_{\text{trial}} > 0$  **then**

| Go to step (iii) to solve for  $\Delta\bar{\varepsilon}_p$

**else**

|  $\Delta\bar{\varepsilon}_p = 0$  and go to step (iv)

**end**

(iii) Use the Newton-Raphson to solve the yield equation for the equivalent plastic strain increment  $\Delta\bar{\varepsilon}_p$ :

$$\sigma_v^{\text{trial}} - (1 - d_{[i]}^{[m+1]2}) 3\mu \Delta\bar{\varepsilon}_p - (1 - d_{[i]}^{[m+1]2}) \sigma_y(\bar{\varepsilon}_p^{[m]} + \Delta\bar{\varepsilon}_p) = 0$$

(iv) Update the constitutive variables

$$\begin{aligned}\boldsymbol{\varepsilon}_e^{[m+1]} &= \boldsymbol{\varepsilon}_e^{\text{trial}} - \sqrt{3/2} \Delta\bar{\varepsilon}_p \frac{\text{dev}(\boldsymbol{\varepsilon}_e^{\text{trial}})}{\||\boldsymbol{\varepsilon}_e^{\text{trial}}||} \\ \hat{p} &= -\frac{\kappa}{J^{[m+1]}} \text{tr}(\boldsymbol{\varepsilon}_e^{[m+1]}) \\ \mathbf{s}^{[m+1]} &= \left[ 1 - (d_{[i]}^{[m+1]})^2 \right] (1/J) 2\mu \text{dev}(\boldsymbol{\varepsilon}_e^{[m+1]}) \\ \bar{\varepsilon}_p^{[m+1]} &= \bar{\varepsilon}_p^{[m]} + \Delta\bar{\varepsilon}_p\end{aligned}$$

(v) **if** *Solve pressure equation* **then**

| Implicitly solve the pressure Poisson's equation:

$$p^{[m+1]} - \mathbb{D}\nabla^2 p^{[m+1]} = \hat{p} - \nabla \cdot (\mathbb{D}\nabla p_{[i]}^{[m+1]})$$

**else**

$$p^{[m+1]} = \hat{p}$$

**end**

(vi) Update the true (Cauchy) stress

$$\boldsymbol{\sigma}^{[m+1]} = \mathbf{s}^{[m+1]} - p^{[m+1]} \mathbf{I}$$

(vi) Solve the phase field equation for  $d$ :

$$\frac{G_c}{2l} (d^{[m+1]} - 4l^2 \nabla^2 d^{[m+1]}) = \mathcal{H}_{[i]}^{[m+1]}$$


---

## 4 Benchmark Cases

This section assesses the performance of the developed finite volume procedures on two benchmark test cases: (i) 2-D axisymmetric notched round bar and (ii) 3-D flat notched bar. In both test cases, a region of localised plastic strain develops at the centre of the specimen, but the levels of triaxiality experienced differ. The cases are presented simultaneously rather than sequentially to allow easier comparison of the material models.

Unless stated otherwise, a global momentum Rhie-Chow scale factor  $\mathcal{R} = 0.01$  is used in all of the following finite volume simulations, and the pressure Rhie-Chow scale factor was  $\mathcal{R}_p = 10^3$ .

**Update:** All simulations were run in parallel on eight CPU cores (Intel Xeon 6152).

Comparisons are made with predictions from finite element software Abaqus and results from the literature. In the Abaqus models, linear interpolation functions are used (Abaqus element code C3D8T for 3-D and CAX4RT for axisymmetry). For reference, single-cell verifications of the proposed material models are provided in Appendix A, providing confidence that the constitutive laws are implemented as intended.

#### 4.1 Geometries and Meshes

The notched round bar (Figure 3(a)) has been widely used for benchmarking plasticity and damage procedures [87–89]. The geometry consists of a 40 mm long round bar of diameter 18 mm with a 4 mm rounded notch. A 2-D axisymmetric model is created, including a horizontal symmetry plane, where a graded structured quadrilateral mesh is employed (Figure 3(b)).

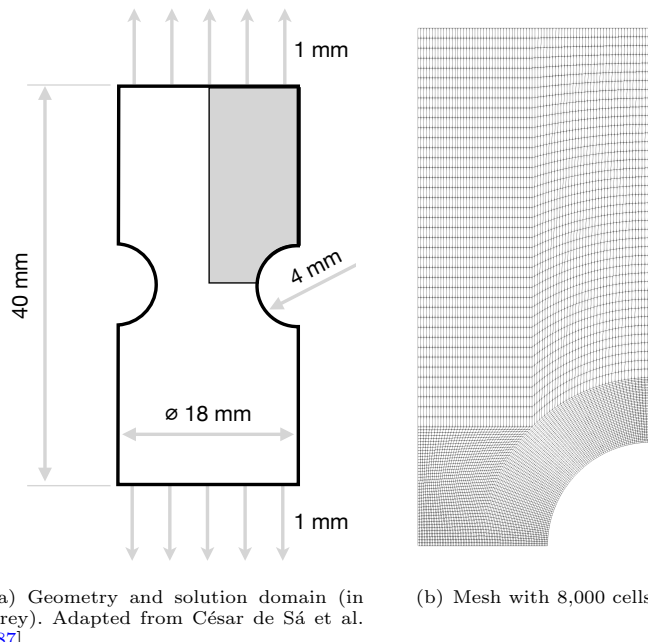


**Fig. 3** Notched round bar geometry and mesh

The 3-D flat notched tensile specimen (Figure 4(a)) is another common test case for assessing damage models [24, 90]. The 3-D geometry consists of  $152.4 \times 25.4 \times 2.37$  mm plate with 4.06 mm diameter side notches. The solution domain comprises one-eighth of the specimen by exploiting three symmetry planes. A graded structured hexahedral mesh is employed with 10,000 hexahedral cells (Figure 4(b)).

#### 4.2 Loading Conditions

For both cases, an axial displacement of 1.0 mm is quasi-statically applied to the upper boundary, resulting in a total elongation of 2 mm applied to the entire sample when accounting for the symmetry planes (Figures 3 and 4). The loading is applied over 1000 equal loading steps, resulting in a time step size of 1 ms.

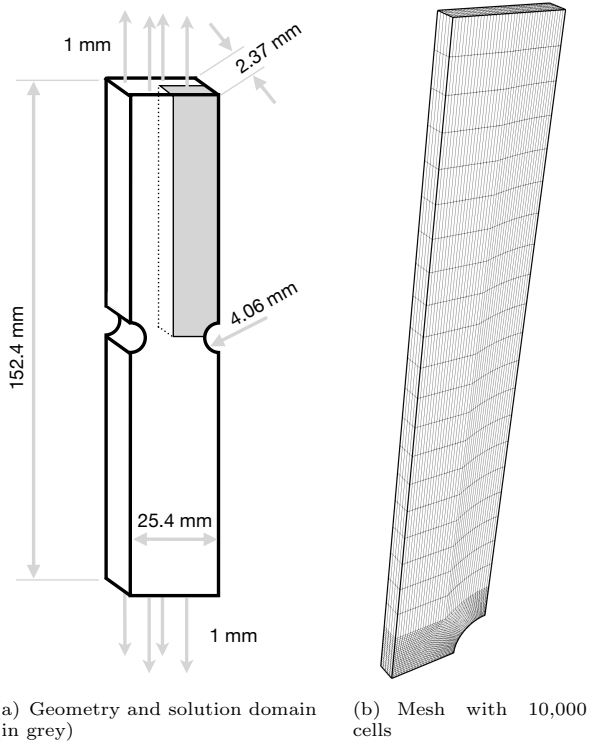


**Fig. 4** Flat notched bar geometry and mesh

An adaptive time-stepping procedure was employed for the Abaqus finite element cases, with a maximum time increment of 1 ms and a minimum of **XXX** ms.

we can easily add a plot of the number of outer iterations

### 4.3 Plasticity Model Verification

Before verifying the damage and fracture models, the implementation of the described plasticity model is verified by comparison with three other procedures:

- The approach of Clancy [11] implemented in OpenFOAM that uses the logarithmic strain and the Mandel stress [56];
- The approach of Cardiff et al. [13] implemented in OpenFOAM, which uses the Green strain tensor (left Cauchy–Green deformation tensor) and the return mapping algorithm described by Simo and Hughes [57];
- The default approach in the finite element software Abaqus, which is based on the Jaumann stress rate.

Verification consists of examining the reaction forces at the loading boundary, and the equivalent plastic strain  $\bar{\varepsilon}_p$ , equivalent stress  $\sigma_v$ , hydrostatic pressure  $p$  and axial stress  $\sigma_{yy}$  (stress in the loading direction) at the centre of the notched round bar and at the coordinate (7.0200) mm for the flat notched bar, where the origin is the geometric centre. These locations have been chosen as the damage is greatest here in the later test cases.

The mesh spacing and time-step size have been chosen so that spatial and temporal discretisation are small for all cases.

#### 4.3.1 Material Parameters

The elastoplastic material parameters for the notched round bar are given in Table 1, while the parameters for the flat notched bar are given in Table 2.

Property	Symbol	Value	Units
Young's modulus	$E$	69	GPa
Poisson's ratio	$v$	0.3	-
Hardening law	$\sigma_y$	$589(10^{-4} + \bar{\varepsilon}_p)^{0.216}$	MPa

**Table 1** Material properties for the notched round bar case

Property	Symbol	Value	Units
Young's modulus	$E$	68.8	GPa
Poisson's ratio	$v$	0.33	-
Hardening law	$\sigma_y$	$320 + 688\bar{\varepsilon}_p$	MPa

**Table 2** Material properties for the flat notched bar case

#### 4.3.2 Reaction Forces

The predicted reaction forces at the loading boundaries (Figures 5) align closely between all approaches. It is worth noting that the reaction forces for both the Clancy [11] implementation and the implementation in this work (which both use the logarithmic strain) are slightly less than the Cardiff et al. [13] and the Abaqus predictions in the latter stages of the deformation. Although the reason for these subtle differences is unclear, the lack of mathematical equivalence between the logarithmic and Green/Jaumann strain approaches may be the cause.

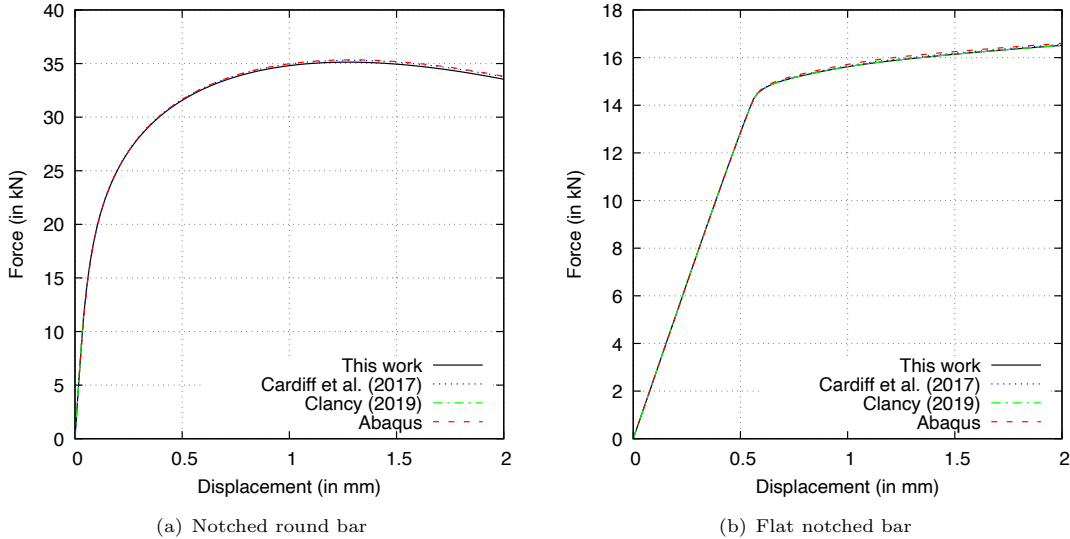


**Fig. 5** Reaction forces at the upper loading boundary for the notched round bar and flat notched bar cases compared with predictions from the methods of Cardiff et al. [13], Clancy [11] and finite element software Abaqus

### 4.3.3 Stresses and Strains

The equivalent plastic strain predictions at the points of interest (see above) agree for all approaches (Figure 6), with the values being marginally greater in the later stages for the finite volume (OpenFOAM) simulations compared with the Abaqus predictions. The value is seen to increase smoothly in the notched round bar case (Figure 6(a)), whereas there is an initial elastic region followed by a steeper slope in the flat notched bar case (Figure 6(b)). These differences have been found to remain as the mesh spacing and time step are reduced, ruling out discretisation error as the cause. A possible reason for the difference is the use of the Jaumann objective rate in Abaqus [91], in contrast to the logarithmic and Green strain approaches used in OpenFOAM.

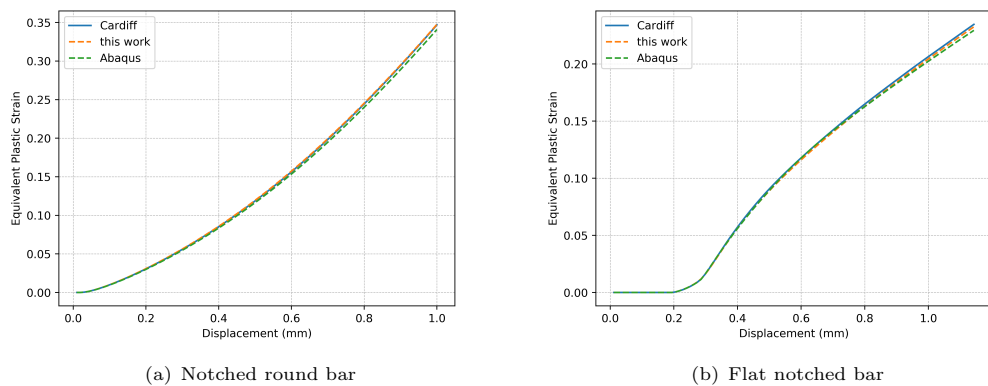


**Fig. 6** Equivalent plastic strain at the specimen centres for the notched round bar and flat notched bar cases

Similarly, the predictions for equivalent stress  $\sigma_v$ , hydrostatic pressure  $p$ , and axial stress (stress in the loading direction)  $\sigma_{yy}$  are shown to agree for the different approaches (Figure ??). Of particular note is the pressure distribution, which is smooth and does not show numerical oscillations,

providing confidence in the proposed pressure smoothing approach (Section 2.2.2). **Images of stress distributions may be better here** point values are already shown above

## 4.4 Lemaitre model

After verifying the elastoplasticity procedure, the notched round and flat bar test cases are examined using the proposed damage models. Comparisons are given against results available in the literature and those generated using Abaqus.

### 4.4.1 Material Parameters

The Lemaitre material parameters for the notched round bar, taken from César de Sá et al. [87], are given in Table 3, while the Lemaitre material parameters for the flat notched bar case are given in Table 4.

Property	Symbol	Value	Units
Young's modulus	$E$	69.9	GPa
Poisson's ratio	$v$	0.3	-
Damage denominator	$S_0$	1.1	MPa
Damage exponent	$b$	1.0	-
Characteristic length	$l_c$	0.6325	mm
Hardening law	$\sigma_y$	$589(10^{-4} + \bar{\varepsilon}_p)^{0.216}$	MPa

**Table 3** Lemaitre material parameters for the notched round bar case

Property	Symbol	Value	Units
Young's modulus	$E$	68.9	GPa
Poisson's ratio	$v$	0.33	-
Damage denominator	$S_0$	0.5	MPa
Damage exponent	$b$	1.0	-
Characteristic length	$l_c$	0.6325	mm
Hardening law	$\sigma_y$	$320 + 688\bar{\varepsilon}_p$	MPa

**Table 4** Lemaitre material parameters for the flat notched bar case

### 4.4.2 Reaction Forces

Comparing the OpenFOAM and Abaqus reaction force predictions (Figure 7), the OpenFOAM and Abaqus predictions can be seen to agree closely. The Abaqus simulations struggled to converge in the rapid crack propagation stage of the flat notched bar case, requiring very small time increments until it eventually crashes before reaching the end time. In contrast, no such issues were encountered with the OpenFOAM simulation. The reason for this difference in convergence behaviour is unclear but may stem from the different solution algorithms employed (Newton-Raphson vs Picard). The Newton-Raphson approach used in Abaqus requires the calculation of the tangent stiffness matrix. For elastoplastic damage models, plastic deformation influences the onset and progression of damage and vice versa. This interaction can result in a significant coupling in the

tangent stiffness matrix, manifesting as non-trivial off-diagonal terms [31], potentially leading to convergence difficulties.

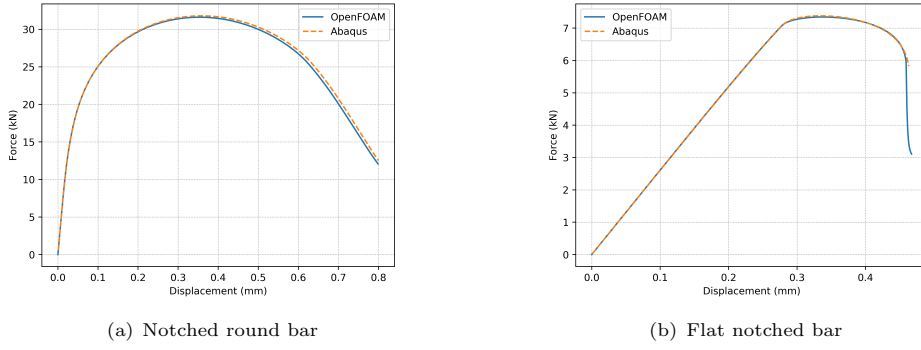


**Fig. 7** Reaction force predictions using the Lemaitre damage model

#### 4.4.3 Stresses, Strains and Damage

Similar to the forces, the local values for damage and equivalent plastic strain can be seen to closely agree between OpenFOAM and Abaqus (Figure 8). Nonetheless, upon examining the figures closely, the OpenFOAM damage and strain are observed to increase slightly quicker than those from Abaqus. This effect can also be observed when viewing the reaction forces (Figure 7) in the previous section. The reason for this is unclear but could be related to the differences in plasticity model formulation, as noted in previous sections.

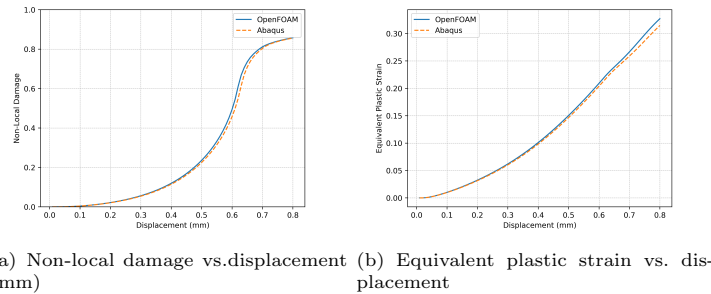


**Fig. 8** Abaqus and OpenFOAM implementations comparison

Figure 9 compares the predicted non-local damage distribution at a loading displacement of 1.2 mm with the predictions provided in César de Sá et al. [87]. Close agreement can be observed between the distributions and values can be observed.

#### 4.4.4 Effect of the $S_0$ Parameter

Here, the simulations are repeated for different values of the material damage parameter  $S_0$  to demonstrate its effect. As the value of  $S_0$  increases, rapid crack propagation occurs later in the

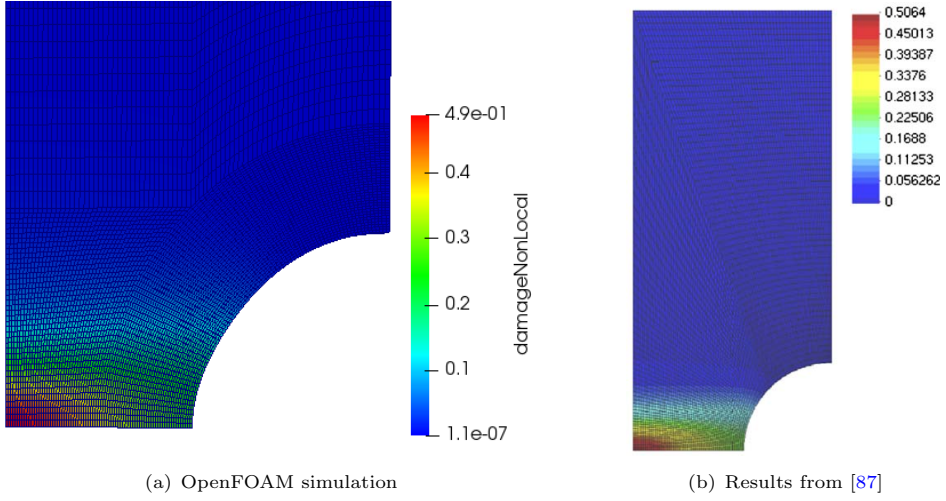


**Fig. 9** Comparison of non-local damage distribution mirror foam results; use same scale

deformation process. The discrepancies between OpenFOAM and Abaqus simulations are larger the later in the deformation process that fracture occurs. Once again,

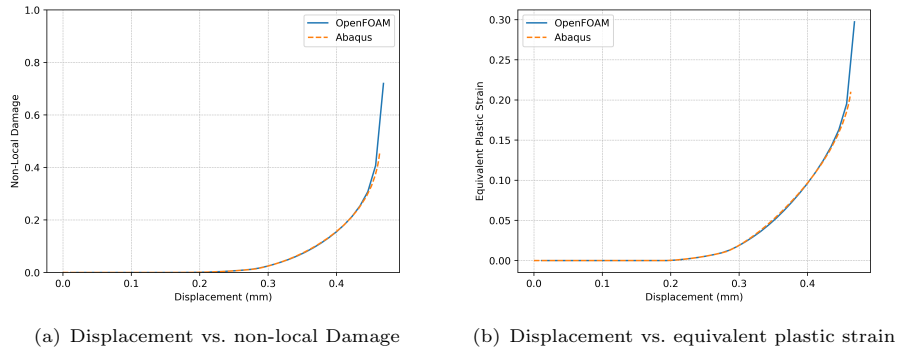


**Fig. 10** Abaqus and OpenFOAM implementations comparison

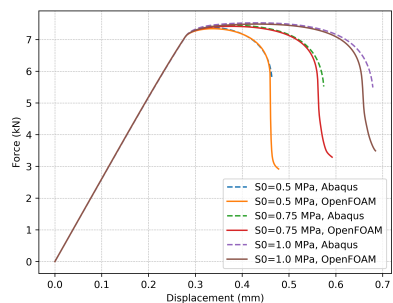


**Fig. 11** Force vs. displacement for different values of  $S_0$

#### 4.4.5 Rhie Chow Case setup

To explore the effect of the Rhie-Chow stabilisation term, various simulations are conducted for different values of the Rhie-Chow scale factor. The values of the Rhie-Chow scale factor used are 0.01, 0.02, 0.05, 0.1, 0.15 and 0.2. The geometry of the cases is the same as in Chapter 5. The cases looked at are as follows: Consider what to add here from comment text and figures

#### 4.4.6 Effect of the Effective Non-Local Damage Parameter

The benefits of this scheme can be seen in Figures ?? and ???. These figures show the results obtained with the novel formulation. For these simulations, the material parameter  $D_c$  is set as 0.55. A more physically realistic damage evolution can be observed, and rapid crack propagation is evident in the force-displacement curve. Such a rapid loss of load-carrying capacity at a certain point for tensile specimens has been observed experimentally [59, 102]. It is worth noting that the fact that the damage is set as 0.99 combined with the diffusive effects of the Rhie-Chow term will still lead to some nonphysical residual force-displacement behaviour of the simulations (e.g. the residual force required for further displacement in Figure ??). Consider what comment figures to add here.

### 4.5 GTN Model

#### 4.5.1 Material Parameters

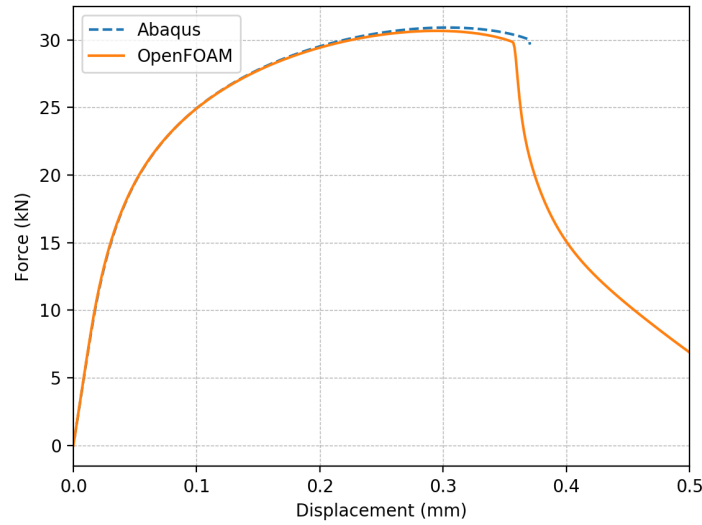
Property	Symbol	Value	Units
Young's modulus	$E$	69	GPa
Poisson's ratio	$\nu$	0.3	-
$q_1$	$q_1$	1.5	-
$q_2$	$q_2$	1	-
$q_3$	$q_3$	2.25	-
Initial porosity	$f_0$	0.002	-
Nucleation strain mean	$\varepsilon_n$	0.15	-
Nucleation strain standard deviation	$S_n$	0.08	-
Void volume fraction parameter	$f_n$	0.2	-
Hardening law	$\sigma_y$	$589(10^{-4} + \bar{\varepsilon}_p)^{0.216}$	MPa

Table 5 GTN material parameters for the notched round bar case

#### 4.5.2 Reaction Forces

In Figure 5.22, it can be seen that the results align well. As with the simulations conducted with the Lemaitre model, quicker localisation can be observed in the OpenFOAM implementation. A feature of this test case is the sharp crack propagation (Figure 5.23). The Abaqus simulation has convergence issues and eventually crashes at a displacement of approximately 0.371 mm. Once again, no convergence issues were encountered in the OpenFOAM simulations. As noted above, the superior convergence abilities of the OpenFOAM simulations are likely because of the segregated solution procedure.

#### 4.5.3 Stresses, Strains and Damage



**Fig. 12** Force vs. displacement

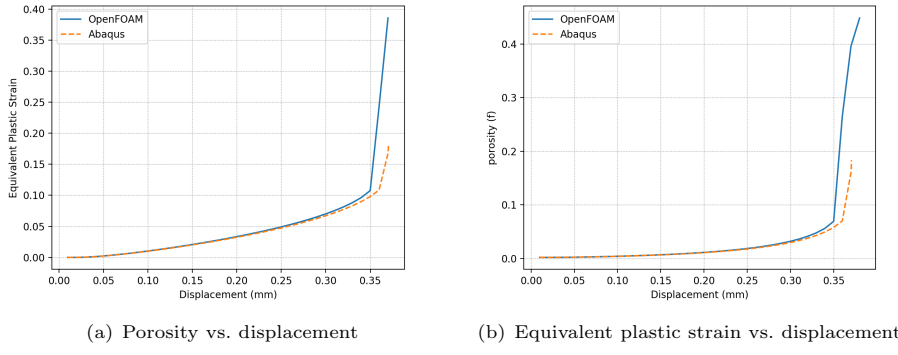


**Fig. 13** Abaqus and OpenFOAM implementations comparison

## 4.6 Phase Field Model

### 4.6.1 Material Parameters

The material properties are given in Table 6.

Property	Symbol	Value	Units
Young's modulus	$E$	68.8	GPa
Poisson's ratio	$\nu$	0.33	-
Critical Fracture Energy	$G_c$	$60 \times 10^3$	J/m <sup>2</sup>
Plastic Threshold	$W_o$	$1 \times 10^7$	MPa
Characteristic Length	$l_c$	0.3226	mm
Hardening law	$\sigma_y$	$320 + 688 \bar{\varepsilon}_p$	MPa

**Table 6** Phase field material parameters for the notched flat notched bar case

### 4.6.2 Reaction Forces

The predicted reaction forces (Figure 14) agree closely with those from Borden et al. [24] and Eldahshan et al. [90]. It is worth noting that the normalised stress reported by Borden et al. [24] before the rapid crack propagation is slightly lower than that obtained here and by Eldahshan et al. [90].

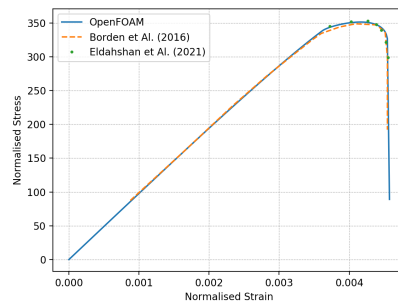


**Fig. 14** Normalised stress vs normalised strain

### 4.6.3 Stresses, Strains and Damage

No comparisons in the thesis: check references to see what can be compared

## 5 Wire Drawing Simulations

### 5.1 The Wire Drawing Process

This section applies the developed damage procedures to the wire drawing metal forming process (Figure 15). The key parameters in the wire drawing process are the die semi-angle  $\alpha$  (in  $^\circ$ ), which is the angle made by the die with the wire axis, and the reduction ratio  $r$  (%), given by

$$r = 100 \times \left( \frac{d_i^2 - d_o^2}{d_i^2} \right) \quad (64)$$

where  $d_i$  is the wire's initial diameter, and  $d_o$  is the die outlet diameter. The final wire diameter tends to be marginally larger than the outlet diameter due to elastic *spring back*.

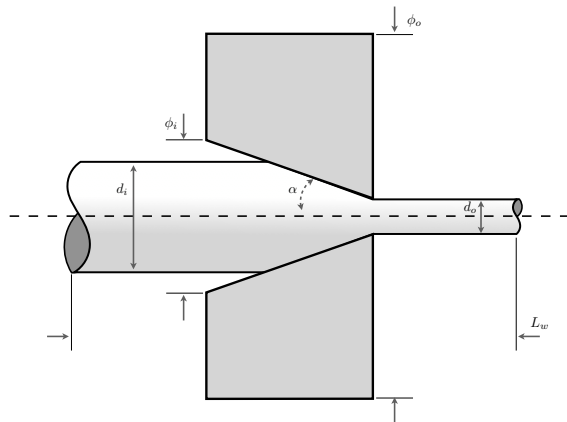


**Fig. 15** Schematic of the axisymmetric wire drawing process with a conical die. See Table 7 for the definition of the symbols.

### 5.2 Comparison of Damage Models for Wire Drawing

In wire drawing, fracture typically originates in the centre of the specimen due to the combination of triaxiality and plastic strain [92–95]. To compare the ability of the damage models to predict this type of damage, a *typical* wire drawing pass is considered, with a reduction ratio  $r$  of 10% and a semi-angle  $\alpha$  of  $6^\circ$  [63]. This case is not expected to display *catastrophic* fracture; however, damage accumulation is expected. The simulations are performed as 2-D axisymmetric with a structured quadrilateral mesh. An average cell width of 0.4 mm is employed, which has been found to minimise mesh errors. Table 7 summarises the geometry and mesh parameters.

Quantity	Symbol	Value	Units
Die inlet diameter	$\phi_i$	16	mm
Die outer diameter	$\phi_o$	20	mm
Die outlet diameter	$d_o$	12.33	mm
Die semi-angle	$\alpha$	6	°
Wire length	$L_w$	30	mm
Wire initial diameter	$d_i$	13	mm

**Table 7** Die and wire geometry for comparing damage modelling approaches. Refer to Figure 15 for interpretation of the parameters.

The wire elastoplastic material parameters, typical of a high-carbon steel, are given in Table 8 [11]. A modified Voce Law [96] (Equation 67) is chosen to describe the plastic hardening law, as Cao [96] found that this law accurately described the hardening behaviour of high carbon steel in tensile, torsion and compression tests.

$$\sigma_y = \sigma_0 + (\sigma_\infty - \sigma_0 + k\bar{\varepsilon}_p)(1 - e^{-\beta\bar{\varepsilon}_p}) \quad (65)$$

The die elastic parameters (Table 9) correspond to tungsten carbide, as is typically used for

Term	Value	Units
Young's modulus	200	GPa
Poisson's ratio	0.3	-
$\sigma_0$	689	MPa
$\sigma_\infty$	1340	MPa
$k$	250	MPa
$\beta$	32.82	-

**Table 8** Wire elastoplastic material parameters, where the hardening behaviour is given by Equation 67

drawing die nibs.

Term	Value	Units
Young's modulus	600	GPa
Poisson's ratio	0.22	-

**Table 9** Die elastic material parameters

A back tension (**how much?**) is applied to the wire upstream boundary, while a total drawing displacement of 30 mm is applied to the downstream wire boundary over 150 ms. Frictional contact (Coulomb coefficient of 0.1) is assumed between the wire and die contact surfaces. All other die surfaces are assumed to have a zero displacement condition, mimicking the steel casings typically used. The Eulerian-type mesh layer addition and removal procedure (Section 2.4) is employed at the wire upstream and downstream boundaries. In the modelling approach adopted here, the entire length of the wire starts at the initial diameter, resulting in an overlap with the die. In the first time step, the contact procedure ‘pushes’ the wire back, enforcing the contact constraints. This procedure has been found to reach quasi-steady-state drawing conditions efficiently; however, it can lead to convergence issues when incorporating damage, particularly in cases with large reduction ratios and high die angles. This issue is ameliorated here by allowing the damage to evolve only after a user-specified drawing displacement, chosen here as 2 mm.

### 5.2.1 Lemaitre Model

Table 10 gives the Lemaitre model wire parameters. Simulations are conducted here, both with and without crack-closure effects. For the Lemaitre model *with* crack-closure effects, the crack-closure parameter is taken to be 0.2 [58, 69, 70].

Property	Symbol	Value	Units
Lemaitre damage denominator	$S_0$	13.5	MPa
Lemaitre damage exponent	$b$	1.0	-
Crack closure parameter	$h$	0.2	-

Table 10 Lemaitre model parameters for wire drawing

Figure 16 provides the predicted Lemaitre damage distributions. It can be observed that without crack-closure effects (upper image in Figure 16), the Lemaitre model gives a somewhat unrealistic damage distribution, with damage being at a maximum away from the centre of the wire. This is because it does not distinguish between positive and negative triaxialities. In contrast, the damage is correctly predicted at a maximum in the centre of the wire for the Lemaitre model with crack-closure effects (lower image in Figure 16). This is because this is where the triaxiality and, relatedly, the positive stress tensor are at a maximum. Both models predict limited damage evolution towards the outer surface of the wire due to the triaxiality cut-off ( $-1/3$ ) for damage evolution.

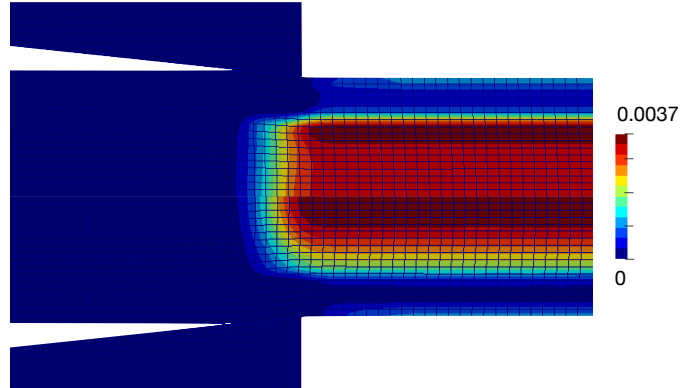


Fig. 16 Predicted damage distribution from the the Lemaitre damage model with (lower) and without (upper) crack-closure effects

### 5.2.2 GTN Model

The GTN model wire parameters are given in Table 11, corresponding to those of a typical high-strength steel.

For the GTN model, porosity growth is negligible for typical wire drawing passes due to the high hydrostatic pressures, making void nucleation the dominant mechanism driving the evolution of the porosity [96]. The GTN model accurately predicts the porosity to be at maximum at the centre of the wire (Figure 17). This is because porosity evolution due to nucleation is only set to occur

Property	Symbol	Value	Units
$q_1$	$q_1$	1.5	-
$q_2$	$q_2$	1	-
$q_3$	$q_3$	2.25	-
Initial porosity	$f_0$	0.002	-
Mean	$\varepsilon_n$	0.03	-
Standard deviation	$S_n$	0.02	-
Volume fraction	$f_N$	0.04	-

**Table 11** GTN model parameters for wire drawing

when the hydrostatic pressure is negative (equation 46). However, there are apparent issues with the assumption of the Gaussian distribution for void nucleation. To illustrate this, the evolution of the equivalent plastic strain and porosity are shown in Figure 18 for a cell near the axis of the wire. It can be observed that the Gaussian assumption leads to the porosity saturating at a certain value, after which it does not evolve. This is unlikely to reflect the true material behaviour [96].

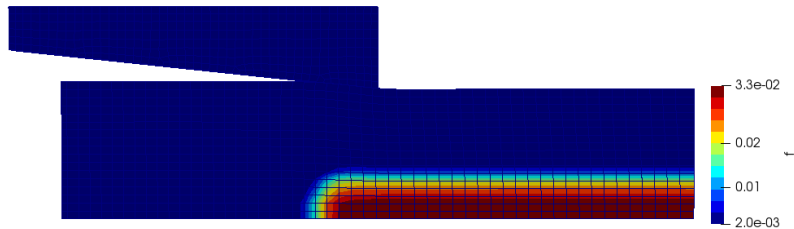


**Fig. 17** Predicted porosity distribution in wire drawing for the GTN model

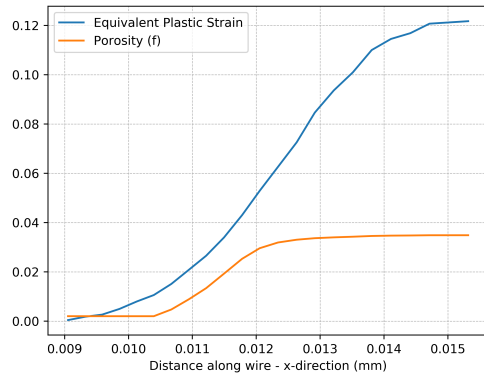


**Fig. 18** Predicted porosity and equivalent plastic strain evolution along the wire axis in the axial (x) direction for the GTN model.

### 5.2.3 Phase Field Model

The phase field model wire parameters are given in Table 12, also chosen to correspond to those of a typical high-strength steel.

The phase field fracture model predicts material degradation to be at its greatest towards the outer surface of the wire (Figure 19). The region with the greatest plastic straining corresponds to the region where material degradation is predicted to be highest. This is contrary to what is

Property	Symbol	Value	Units
Critical fracture energy	$G_c$	1	MJ/m <sup>2</sup>
Plastic work threshold	$W_o$	0	J
Characteristic length	$l$	0.3266	mm

**Table 12** Phase field fracture model parameters for wire drawing

expected. The current phase field model does not distinguish between tensile and compressive stress states for the plastic contribution towards crack growth, leading to this unrealistic behaviour.

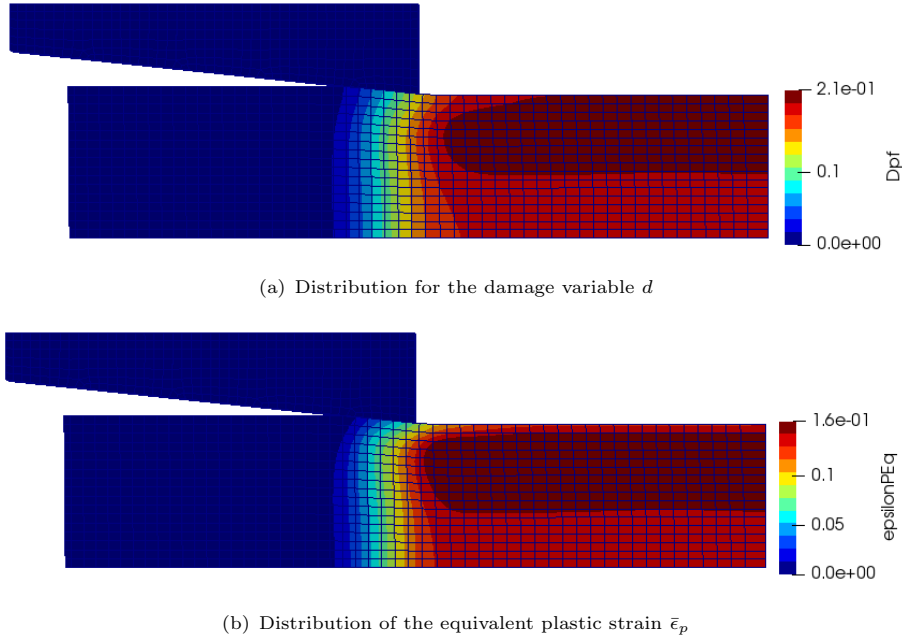


**Fig. 19** Predicted damage and equivalent plastic strain fields in wire drawing for the phase field model.

#### 5.2.4 Comparison of Damage Models Approaches

Along with the limitations in the GTN and phase field models described in the previous section, other factors make them unsuitable for further investigation in predicting fracture in wire drawing processes. The phase field fracture model requires a relatively fine mesh [24], making it computationally expensive. The GTN model requires the calibration of multiple parameters, which is not feasible given the data available for the cases that will be looked at here. To rigorously calibrate these parameters, the characterisation of each stage of ductile damage requires the continuous monitoring of void nucleation, growth and coalescence during deformation. This is possible (for example, using X-ray tomography measurements such as in Thuillier et al. [97] and Fansi et al. [98]), but is far more demanding than required of the Lemaître-type models. Consequently, Lemaître-based damage models with crack-closure effects are chosen here for further evaluation.

### 5.3 Prediction of Chevron Cracks

To test the Lemaître models further, their ability to predict *chevron cracks* is examined in this section. Chevron cracks, also known as central burst defects, are common defects that occur at the wire centre in drawing (Figure 20).

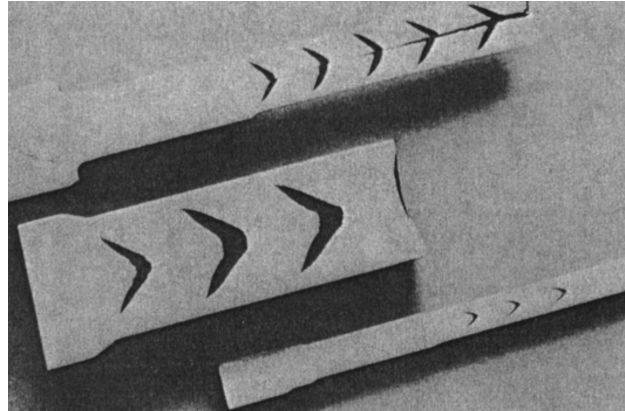


**Fig. 20** Chevron cracks in steel rods, similar to those that can occur in drawn wires [103]

A reduction of  $r = 20\%$  and a die semi-angle of  $\alpha = 10^\circ$  are chosen, where all geometric parameters are given in Table 13.

Die inlet diameter	$\phi_i$	16	mm
Die outer diameter	$\phi_o$	20	mm
Die outlet diameter	$d_o$	11.627	mm
Die semi-angle	$\alpha$	10	$^\circ$
Wire length	$L_w$	30	mm
Wire initial diameter	$d_i$	13	mm

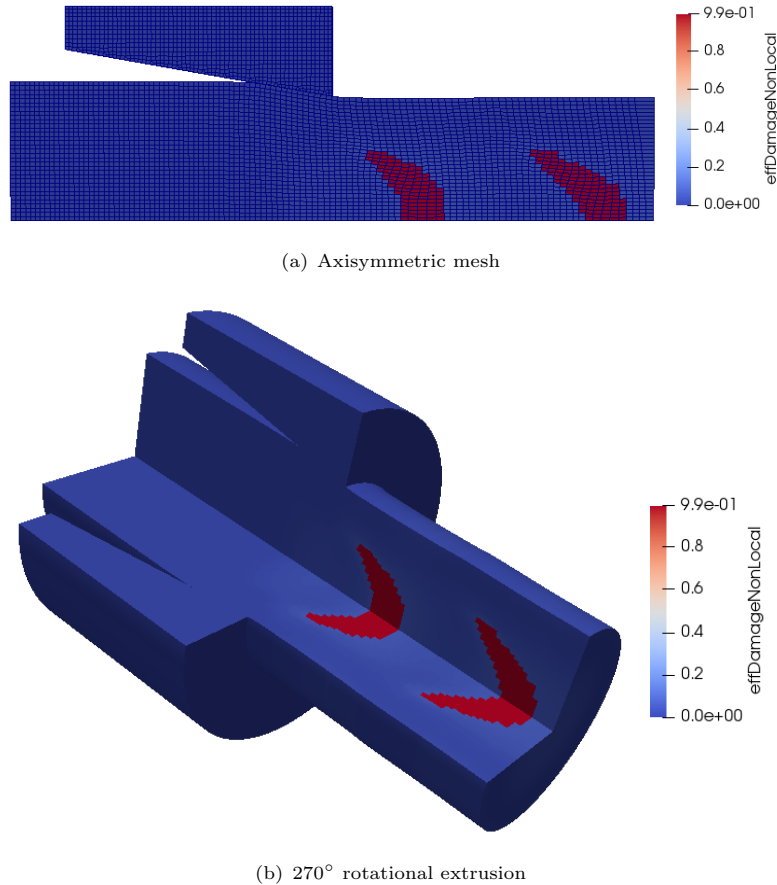
**Table 13** Die and wire geometry used for the chevron crack predictions.

Table 14 gives the assumed wire elastoplastic Lemaître properties. These properties have been chosen with the drawing reduction and angle to be in a drawing regime that produces chevron cracks. Table 9 gives the die elastic properties. Where did these props come from?

Property	Symbol	Value	Units
Young's modulus	$E$	200	GPa
Poisson's ratio	$v$	0.33	-
Lemaître damage denominator	$S_0$	15	MPa
Lemaître damage exponent	$b$	1.0	-
Critical damage	$D_c$	0.052	-
Characteristic length	$l_c$	0.325	mm
Initial yield stress	$\sigma_0$	600	MPa
Asymptotic yield stress	$\sigma_\infty$	1280	MPa
Hardening parameter	$k$	250	MPa
Hardening parameter	$\beta$	43.44	-

**Table 14** Wire material parameters for the chevron crack simulation. The hardening behaviour is given by Equation 67.

Using the developed effective non-local damage scheme, the accurate modelling of chevron cracks is evident in Figure 21. The characteristic semi-lunar-shaped cracks are found to occur at a fixed frequency and continue to form as long as the drawing continues. From the modelling perspective, it has been found that if the local damage field  $D$  is not restricted when  $\bar{D}_{eff} > D_c$ , as described in Section 3.4.2, the non-local damage field grows excessively, resulting in the over-prediction of damage. Consequently, rapid crack propagation ensues, and the formation of chevron cracks is not predicted. Hence, the inclusion of such a damage-limiting procedure has been found to be crucial in the prediction of these types of defects.



**Fig. 21** Chevron cracks in wire drawing

## 5.4 Fracture Prediction in a Drawing Series

### 5.4.1 Drawing Series Overview

In this final section, the experimental wire drawing series from Roh et al. [63] is used to investigate the ability of the Lemaitre-based damage models to predict fracture. Data is available for die half-angles  $\alpha$  from 2 to 16°, and reduction ratios  $r$  from 20 to 36%. The initial wire diameter was 13 mm. Table 15 summarises the experimental drawing test data available for the examined high-carbon steel wire, where tests which displayed catastrophic wire fracture are indicated with the symbol  $X$ .

Reduction $r$ (%)	Drawing Die Half-Angle $\alpha$ ( $^{\circ}$ )	Fracture
20	2	-
	4	-
	6	-
	8	-
	10	-
	12	X
	14	X
	16	X
36	4	-
	6	-
	8	-
	10	-
	12	X
	14	X
	16	X

**Table 15** Experimental high-carbon steel wire drawing series data from Roh et al. [63], where tests which displayed catastrophic wire fracture are indicated with the symbol X

A 30 mm long wire was used for drawing simulations, aside from the cases where  $r = 36\%$ ,  $\alpha = 4^{\circ}$  and  $r = 20\%$ ,  $\alpha = 2^{\circ}$ . In these cases, a longer 50 mm wire was used to ensure minimum upstream and downstream boundary effects. The die and wire geometry is summarised in Table 16. An average cell width of 0.25 mm was found to be sufficient to minimise mesh errors. The coefficient of friction was taken as  $\mu = 0.08$ , as determined in Roh et al. [63]. Neither the die's specific geometry nor the die's material properties are specified in Roh et al. [63], so a conical die is assumed here with die material parameters taken from Clancy [11], corresponding to tungsten carbide. A total drawing displacement of 30 mm is applied to the wire downstream boundary in increments of 0.1 mm with a time step size of 0.5 ms (the total simulation time was 150 ms). A back tension of XXXX was applied to the wire upstream boundary. As before, the damage can only evolve after a drawing displacement of 2 mm to avoid localisation in the initial time steps.

Die inlet diameter	$\phi_i$	16	mm
Die outer diameter	$\phi_o$	20	mm
Die outlet diameter	$d_o$	[11.627, 10.4]	mm
Die semi-angle	$\alpha$	[2, 4, 6, 8, 10, 12, 14, 16]	$^{\circ}$
Wire length	$L_w$	[30, 50]	mm
Wire initial diameter	$d_i$	13	mm

**Table 16** Die and wire geometry used for the drawing series analyses.

In the models presented here, the non-local gradient equation is not incorporated as localisation behaviour is limited due to the low calibrated value of  $D_c$ , and hence, it would not significantly change the results.

#### 5.4.2 Material Model Calibration

To calibrate the elastoplastic and Lemaitre parameters, tensile test data provided in Roh et al. [63] is used (Figure 22). The calibration procedure follows that of Masse [8], where the plastic hardening law is first calibrated against the experimental force-displacement data up to the point where necking is observed ( $\approx 6.5\%$  engineering strain). Subsequently, the damage parameters are calibrated while the elastoplastic parameters are fixed. The calibration procedure is simplified by

separating out the calibration of the plastic hardening law and the damage parameters, and the risk of over-fitting is reduced. The Young's modulus (200 GPa), Poisson's ratio (0.3) and initial yield stress (689 MPa) are taken directly from Roh et al. [63].

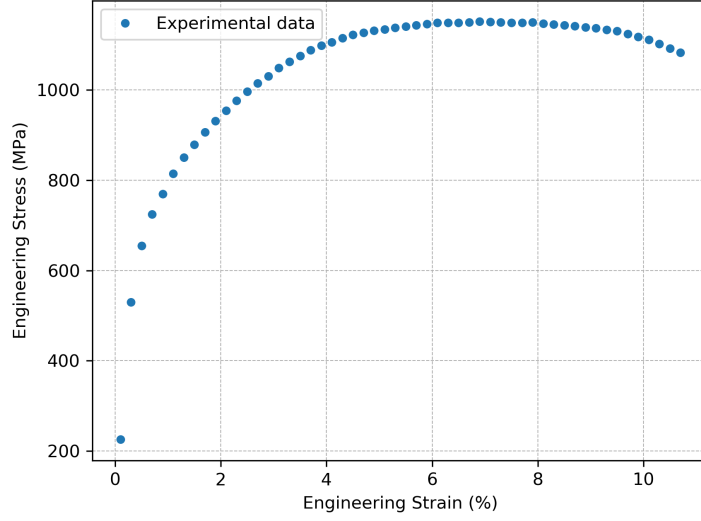


**Fig. 22** Tensile test experimental data from Roh et al. [63]

A combined global-local approach is taken to calibrate the elastoplastic and damage parameters. Initially, 50 sets of values for  $\sigma_\infty$ ,  $k$  and  $\beta$  (Equation 67) are taken from the range of values given in Table 17 using Latin hypercube sampling [99]. Each of these sets of values is used to simulate a tensile test. The force-displacement curves from each simulation are then compared to the experimental data up to 6.5% engineering strain (onset of necking). The results with the minimum difference from this *global* sampling are then further optimised using the *local* Nelder-Mead method [100] to refine the material parameters. Table 17 gives the final optimised values. Here, two forms of the Lemaitre model are compared: (i) the classic form, where the  $S$  parameter is a constant, and (ii) the form proposed in Equation 33, which introduces a triaxiality dependence to the  $S$  parameter.

Term	Range		Optimal Value	Units
	Lower	Upper		
$\sigma_\infty$	1.1	1.5	1.34	GPa
$k$	50	500	104	MPa
$\beta$	25	80	32.82	-

**Table 17** Elastoplastic parameter search ranges and optimal calibrated values

Once the elastoplastic parameters have been fit, the Lemaitre damage parameter  $S_0$  is determined. To do this, 50 values are sampled in the range in Table 18. For the classic and proposed Lemaitre laws, tensile test simulations are conducted for each value of  $S_0$ , with the elastoplastic parameters held constant at the previously found optimal values. As before, the results with the

minimum difference from this *global* sampling are then further optimised using the *local* Nelder-Mead method [100] to refine the material parameters (Table 18). Finally, the critical damage parameter  $D_c$  is set as the maximum value for the simulated damage obtained at the failure strain (10.7% engineering strain) [76].

Term	Range		Optimal Value		Units
	Lower	Upper	Classic	Proposed	
$S_0$	5	25	13.81	14.29	MPa
$D_c$	-	-	0.078	0.087	-

**Table 18** Lemaitre damage parameter search ranges and optimal calibrated values, where the proposed law corresponds to Equation 33.

The resultant force-displacement curves obtained using the calibrated parameters are given in Figure 23, and the optimal calibrated parameters in Tables 17 and 18.

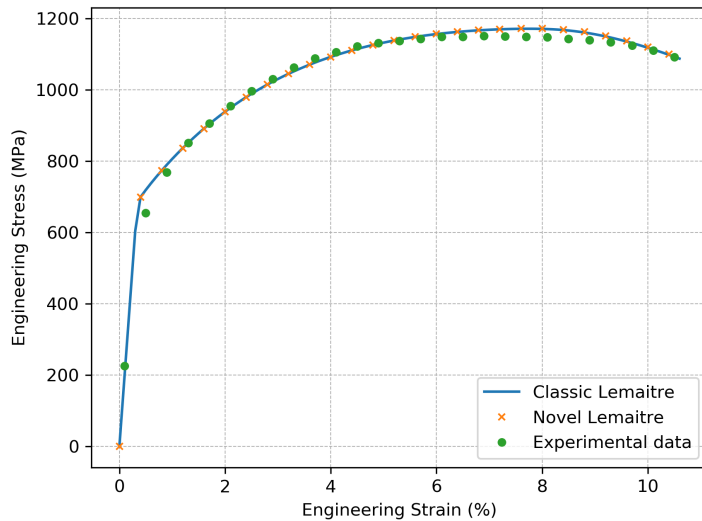


**Fig. 23** Comparison of the experimental tensile test curve and the calibrated elastoplastic Lemaitre material laws. The ‘Novel Lemaitre’ model corresponds to Equation 33.

### 5.4.3 Predicted Evolution of Damage

For all of the cases simulated here, the damage is at a maximum towards the centre of the specimen. As an example, the predicted damage distribution for the case where  $r = 36\%$ ,  $\alpha = 6^\circ$  using the classic Lemaitre damage evolution equation is shown in Figure 24. The greatest damage occurs at the centre of the wire because this is where the triaxiality and, relatedly, the positive stress tensor are greatest. The evolution of the equivalent plastic strain, triaxiality and damage for a given cell near the wire axis is provided in Figure 25. It can be observed that the damage evolution primarily occurs with the increase in triaxiality towards the latter stage of its plastic straining.

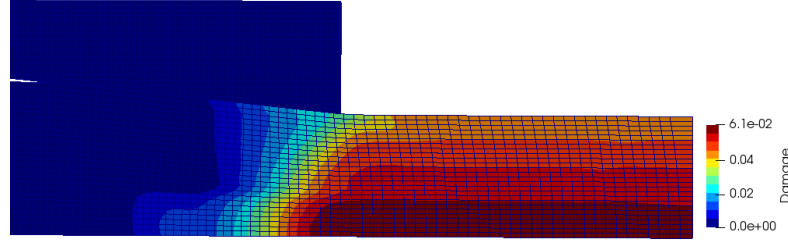


**Fig. 24** Distribution of damage for  $r = 36\%$ ,  $\alpha = 6^\circ$

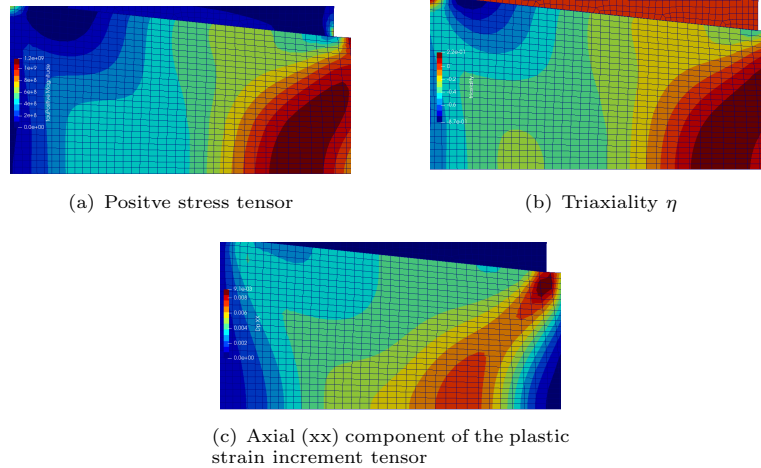


**Fig. 25** Predicted distribution of fields for the  $r = 36\%$ ,  $\alpha = 6^\circ$  wire drawing case

#### 5.4.4 Fracture Prediction

To determine whether a fracture is predicted to occur, the accumulated damage at the wire centre axis is compared with the critical damage  $D_c$  (Figure 26). Fracture can be expected to occur when the quantity  $D/D_c$  becomes greater than or equal to 1. Figure 26 shows that both the classic and the proposed formulations of the Lemaitre model are reasonably consistent with the experimental results. The classic model accurately predicts fracture for the 20% reduction cases but overpredicts fracture in the 36% reduction cases. The novel Lemaitre-based model slightly underpredicts fracture in both the 20% and 36% reduction cases, with a value for  $D$  that is 90.4% and 90.8% of  $D_c$ , respectively.

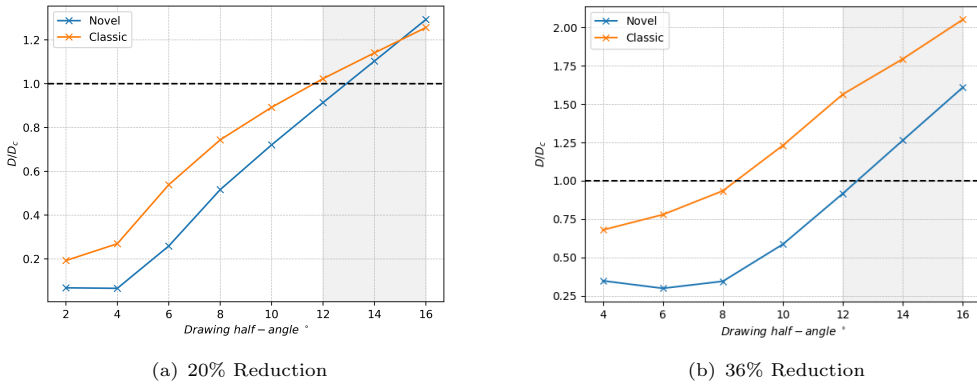


**Fig. 26** Comparison of predicted and experimental fractures. The shaded region indicates where fractures occurred in experiments, corresponding to the  $X$  symbols in Table 15.

## 6 Conclusions

This article presents for the first time the implementation of three popular ductile damage models within a segregated, cell-centred finite volume framework. Verification of the proposed procedures is given against popular benchmark cases from the literature, where the proposed approach has shown a robust ability to solve the highly nonlinear coupled equations. Subsequently, the ability of the examined damage models to predict damage accumulation in the wire drawing process is assessed. The main conclusions of the work are:

- An implicit, segregated solution algorithm with Picard iterations has been shown to be robust for damage modelling.
  - Novel Eulerian-style layer addition and removal boundary conditions are demonstrated to be capable of simulating the continuous wire drawing process.
  - Lemaitre-type models are more appropriate for predicting damage in wire drawing processes than current formulations of GTN and phase field models.
  - A proposed incorporation of triaxiality dependency to the Lemaitre  $S$  parameter improves the model's predictive capabilities for wire drawing.
  - When incorporating a non-local damage approach, limiting the effective damage parameter is important.
  - Care must be taken when scaling the Rhie-Chow stabilisation term in regions of damage and plasticity to minimise mesh and time step errors;
  - A combined global-local optimisation is suitable for calibrating elastoplastic and damage parameters from experimental test data.

Regarding the prediction of damage in a wire drawing series, although the predictions generally aligned with the experimental data, limitations in the modelling approach exist: (i) Prediction of catastrophic fracture is relatively sensitive to the critical damage  $D_c$  parameter determined from tensile test data; (ii) The assumption of Coulomb friction may be limiting in wire drawing, where hydrodynamic lubrication is known to occur; (iii) In the authors' opinion, the strong association between the positive stress tensor  $\tau^+$  and the triaxiality  $\eta$  at low triaxiality values ( $< 0.33$ ), which occurs in wire drawing, has been neglected. Further incorporation of the positive stress tensor into the damage evolution law may potentially better describe material fracture behaviour.

**Acknowledgments.** This work has emanated from research conducted with the financial support of/supported in part by a grant from Science Foundation Ireland (SFI) under Grant number RC2302\_2. Philip Cardiff gratefully acknowledges financial support from the Irish Research Council through the Laureate program, grant number IRCLA/2017/45, and the European Research Council (ERC) under the European Union’s Horizon 2020 research and innovation programme (Grant agreement No. 101088740). Vikram Pakrashi would also like to acknowledge FlowDyn RDD/966 and SiSDATA EAPA\_0040/2022. Additionally, the authors want to acknowledge project affiliates, Bekaert, through the Bekaert University Technology Centre (UTC) at University College Dublin ([www.ucd.ie/bekaert](http://www.ucd.ie/bekaert)), I-Form, funded by SFI Grant Number 16/RC/3872, co-funded under European Regional Development Fund and by I-Form industry partners, NexSys, funded by SFI Grant Number 21/SPP/3756, and the DJEI/DES/SFI/HEA Irish Centre for High-End Computing (ICHEC) for the provision of computational facilities and support ([www.ichec.ie](http://www.ichec.ie)). Finally, part of this work has been carried out using the UCD ResearchIT Sonic cluster funded by UCD IT Services and the UCD Research Office.

## Appendix A Appendix: Single Cell Verifications

To add a further point of comparison, the non-local Lemaitre damage model was also implemented in Abaqus/Standard, a commercial finite element-based software. This was implemented through a user subroutine (UMAT). The Abaqus software has an inbuilt GTN model that we can also use to compare with.

To implement the diffusion equation for the non-local Lemaitre damage model, the approach laid out in Azinpour et al. [104] is employed in this work. In Azinpour et al. [104], the authors use the Abaqus' software ability to solve the steady-state heat conduction diffusion equation in coupled temperature-displacement problems.

$$q = -k\nabla^2 T \quad (\text{A1})$$

where  $q$  is the source term,  $k$  is the material's conductivity and  $T$  is the temperature.

This equation is made compatible with the non-local gradient equation as shown in table 5.1.

Field	Field variable	Diffusion coefficient	Flux term	Source term
Temperature	$T$	$k$	$\nabla^2 T$	$q$
Non-local damage	$\bar{D}$	$l_c^2$	$\nabla^2 D$	$\bar{D} - D$

**Table A1** Analogous set-up of the heat equation and non-local gradient equation

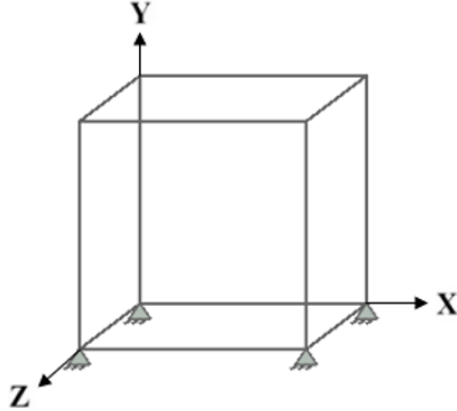


**Fig. A1** one element case

In order to verify the implementation of these models, tests are conducted on an element of geometry  $1\text{ mm} \times 1\text{ mm} \times 1\text{ mm}$  (Figure 5.1). The elements used in the solids4Foam toolbox have previously been validated through a patch test [105]. In this test case, a displacement is applied in the  $y$  direction to the top boundary of the element.

### A.1 Lemaitre model

A displacement of  $0.2\text{ mm}$  is applied with mechanical properties described in Table 5.2. These mechanical properties are taken from Autay et al. [106].

Property	Symbol	Value
Young's modulus	$E$	200 GPa
Poisson's ratio	$v$	0.3
Lemaitre damage denominator	$S_0$	0.5 MPa
Lemaitre damage exponent	$b$	1.0
Hardening law	$\sigma_y$	$200 + 10^3 \times \bar{\varepsilon}^p$ MPa

**Table A2** Material properties for Lemaitre one cell test

The results gained from simulations in OpenFOAM and Abaqus are compared with the analytical relationships derived in Doghri [107] in Figure 5.2. The analytically derived relationship for the damage  $D$  as a function of the equivalent plastic strain  $\bar{\varepsilon}^p$  is given by

$$(1 - D)^2 = 1 - \frac{\sigma_{y0}^2}{3ES_0} \frac{\sigma_{y0}}{h} \left[ \left( 1 + \frac{h}{\sigma_{y0}} \bar{\varepsilon}^p \right)^3 - 1 \right] R_v \quad (\text{A2})$$

where  $\sigma_{y0}$  and  $h$  are constants in the hardening law  $\sigma_{y0} + h(\bar{\varepsilon}^p)$ .  $R_v$  is given by:

$$R_v = \frac{2}{3}(1 + v) + 3(1 - 2v)(\eta) \quad (\text{A3})$$

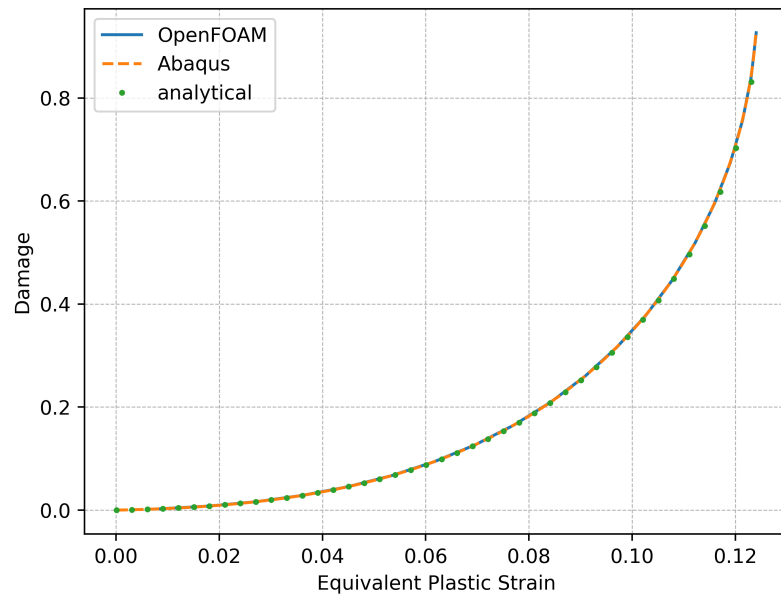
where the triaxiality  $\eta = 0.33$  for a uniaxial tensile test.

The analytical relationship for the equivalent stress  $\sigma_{eq}$  is also provided

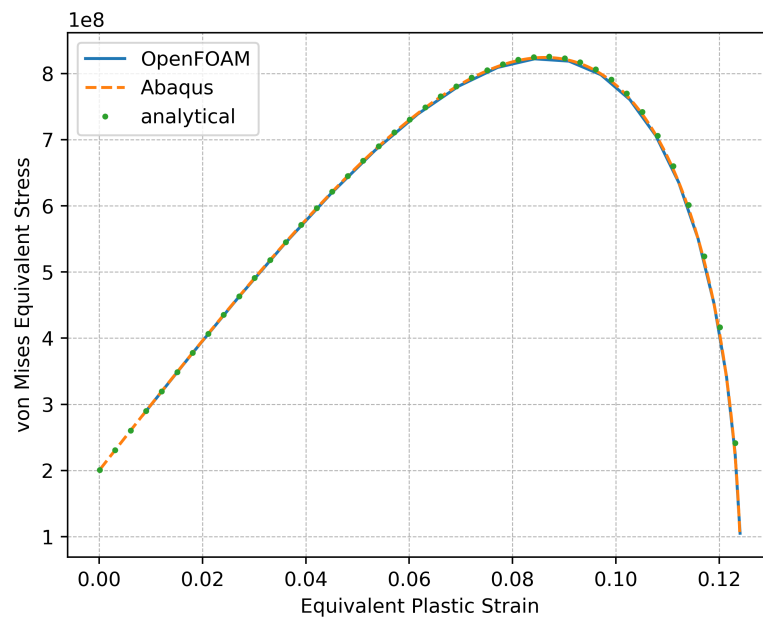
$$\sigma_{eq} = (1 - D)(\sigma_{y0} + h(\bar{\varepsilon}^p)) \quad (\text{A4})$$

It can be observed that the damage increases in an exponential manner with respect to the equivalent plastic strain. This is due to the fact that with the material constant  $b = 1$ , the Damage increases with the square of the effective von Mises equivalent stress (equation 30).

The plastic strain in the Y direction  $\varepsilon_{yy}^p$  is also given as a function of the equivalent plastic strain  $\bar{\varepsilon}^p$  and compared with the results obtained by Doghri [107] (Figure 5.3).



(a) Damage vs. equivalent plastic strain



(b) Equivalent stress vs. equivalent plastic strain

**Fig. A2** Comparison between OpenFOAM, Abaqus and analytically derived relationships

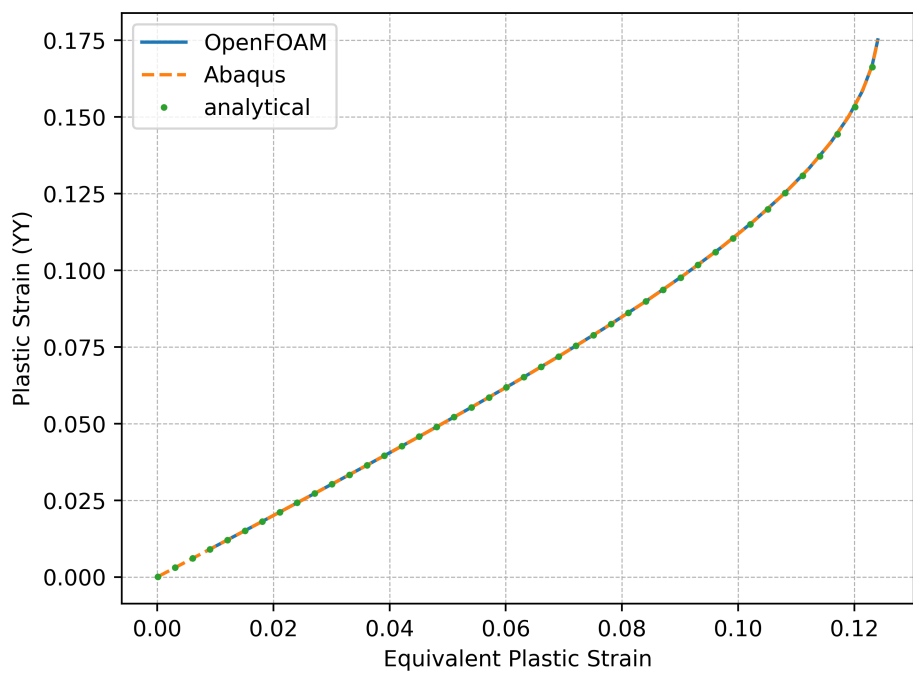


**Fig. A3** Plastic strain (YY) vs. equivalent plastic strain

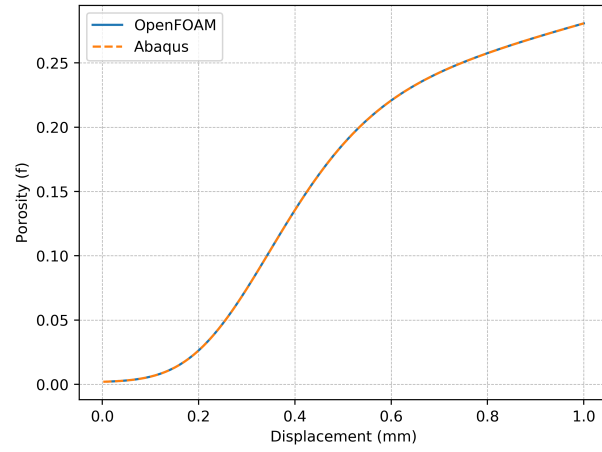
## A.2 GTN model

Property	Symbol	Value
Young's modulus	$E$	200 GPa
Poisson's ratio	$\nu$	0.3
$q_1$	$q_1$	1.5
$q_2$	$q_2$	1
$q_3$	$q_3$	2.25
Initial porosity	$f_0$	0.002
Mean	$\bar{\varepsilon}_n$	0.3
Standard deviation	$S_n$	0.1
Volume fraction	$f_N$	0.2
Hardening law	$\sigma_y$	$400 + 300 \times \bar{\varepsilon}^p$ MPa

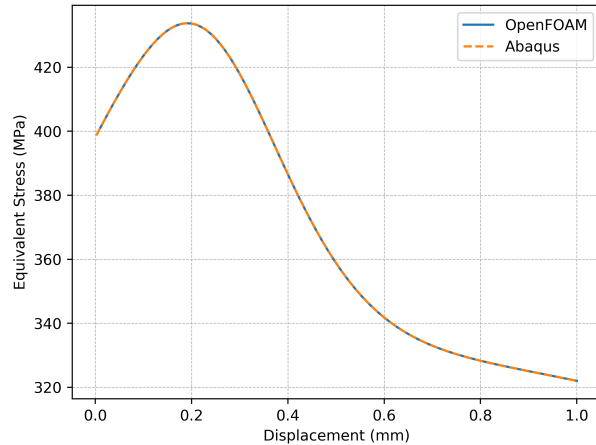
**Table A3** Material properties for GTN one cell test

In this section, the results for the GTN model implemented in OpenFOAM are compared with those obtained from the inbuilt GTN model in Abaqus. The material properties used are displayed in Table 5.3. The GTN model in Abaqus does not allow for the inclusion of porous failure criteria (equation 43) in Abaqus/Standard so this feature of the GTN model was neglected. The results are compared in Figure 5.4.

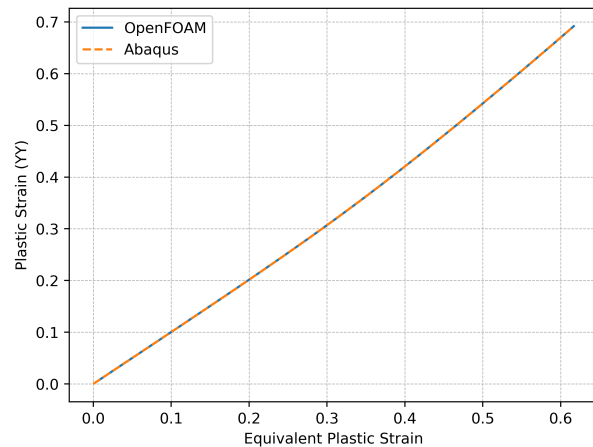
It is clear that there is strong agreement between Abaqus and the OpenFoam implementation. It is notable that the rate of porosity growth declines towards the latter stages of the deformation in Figure 5.4 a). This is due to the fact that the porosity growth due to the nucleation of voids is assumed to follow a Gaussian distribution (equation 46). As will be discussed in chapter ??, this assumption is unlikely to be an accurate description of material behaviour.



(a) Porosity vs. displacement



(b) Equivalent stress vs. displacement



(c) Plastic strain in the Y direction vs. Equivalent plastic strain

**Fig. A4** Comparison between OpenFOAM and Abaqus

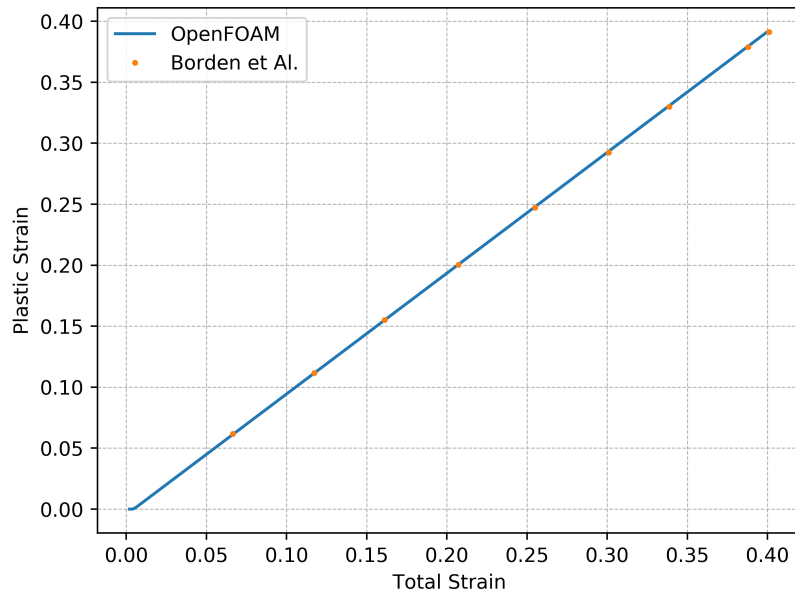
### A.3 Phase field fracture

Property	Symbol	Value
Young's modulus	$E$	68.8 GPa
Poisson's ratio	$\nu$	0.33
Critical fracture energy	$G_c$	$138 \times 10^6 \text{ J/m}^2$
Plastic work threshold	$w_0$	$10^6 \text{ J}$
Characteristic length	$l$	2 m
Hardening law	$\sigma_y$	$320 + 688 \times \bar{\varepsilon}^p \text{ MPa}$

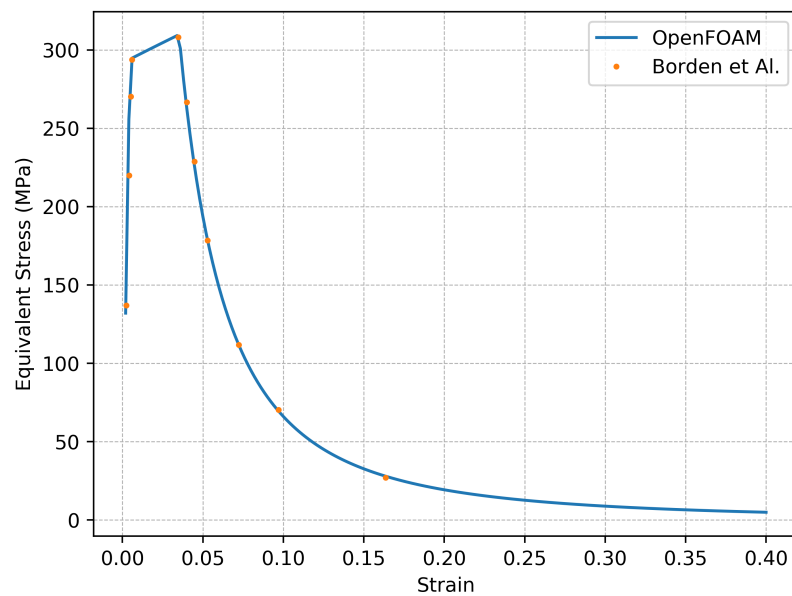
**Table A4** Material properties for phase field fracture one cell test

Here the results obtained from a one-cell test are compared with those obtained by Borden et al. [24] in Figure 5.5.

In this test case, the cell undergoes a rapid loss of load-carrying capacity (Figure 5.6). This is due to the fact that after the plastic work threshold is exceeded, there is a rapid increase in the plastic strain energy contribution to the crack-driving force  $\mathcal{H}$  and therefore growth of the phase field variable  $d$ . The combination of this and the fact that the crack degradation function is proportional to the square of the phase field ( $g_e(d) = (1 - d)^2$ ) leads to the swift reduction in the equivalent stress.

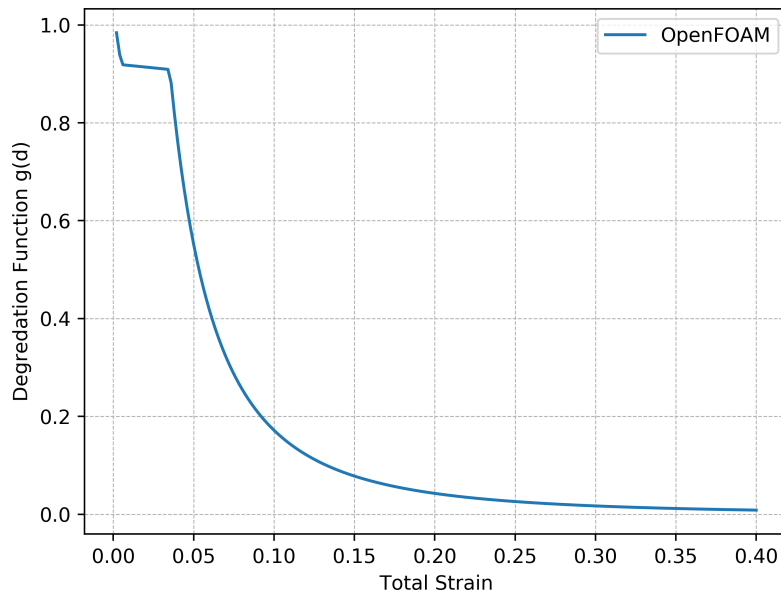


(a) Plastic strain vs. total strain

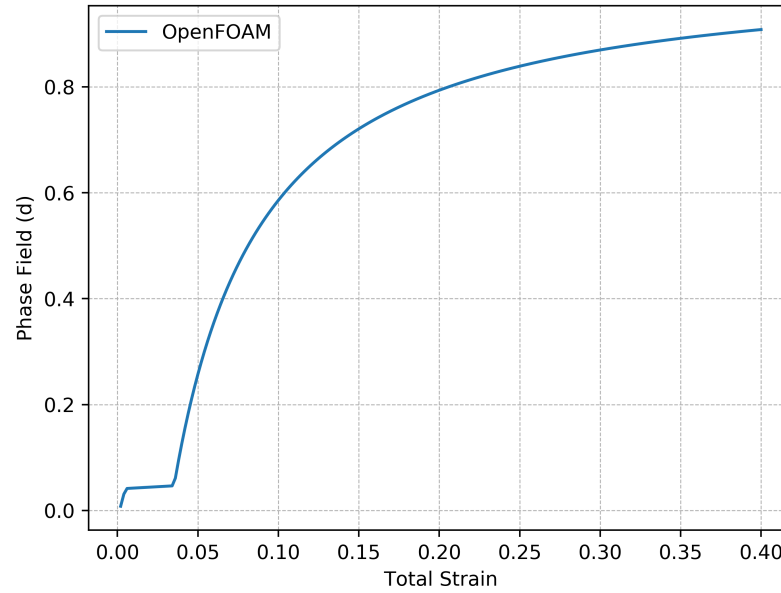


(b) Equivalent stress vs. total strain

**Fig. A5** Comparison between OpenFOAM and [24]



(a) Crack degradation function  $g(d)$  vs. total strain



(b) Phase field ( $d$ ) vs. total strain

**Fig. A6** Evolution of  $d$  and the crack degradation Function

## Appendix B Phase Field Model Updated-to-Total Lagrangian Transformation

Given that the mesh is moved to the updated configuration after each time step, the non-local equation is solved with respect to this updated mesh configuration. However, sometimes it may be preferred to solve the non-local equation with respect to the initial mesh configuration.

It's worth noting however that the results from the non-local equation will differ if the non-local gradient equation is solved with respect to the initial configuration  $\Omega_0$ . If the non-local equation is solved with respect to the updated configuration, then in tension the non-local damage will tend towards the local damage as the distance between the cell centres will increase. Conversely, in compressive states, the distances between cell centres will decrease leading to greater diffusion in the region of a damaged cell. In order to illustrate this, simulations on a one-dimensional bar of length 10mm were performed. An imperfection is placed at the centre of the bar so that here the local damage  $D = 1.0$ . In all other cells  $D = 0$ . Both 20% compressive and tensile strains were applied. It can be seen in Figure B7 how the distribution of the non-local damage is therefore altered as the bar undergoes tension and compression

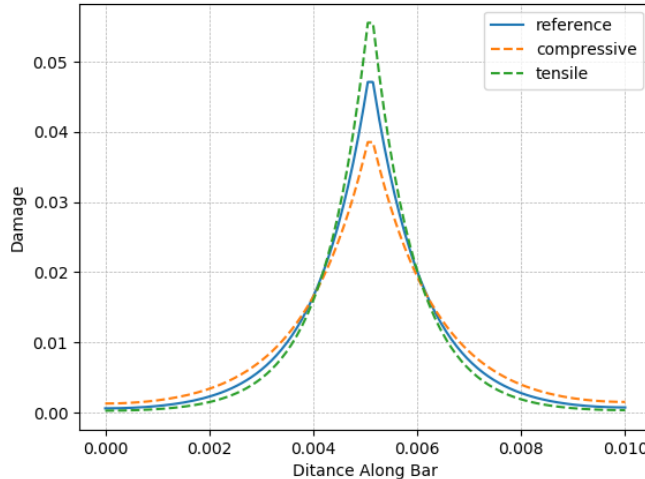


**Fig. B7** Non-local damage along the original bar length

It remains a matter of debate in the literature as to whether solving this equation with respect to the initial or updated configuration is preferable [73]. Steinmann [108] has argued that the fact that the non-local damage will tend towards the local damage (in an object undergoing tensile loading) is an argument for solving with respect to the initial configuration to ensure that the mesh independence of the solution remains strong. However, he also noted that this may not be physically realistic as it is not likely the case that a material's non-local properties are completely independent of its deformation path.

In order to ensure that solving the non-local gradient equation with respect to the initial configuration is possible, within the context of an updated Lagrangian solid model, a mathematical and algorithmic approach was developed in this work. This approach allows for the solving of

the non-local gradient equation with respect to the initial configuration within the context of an updated Lagrangian solid model framework.

To begin, the strong integral form of the non-local equation with respect to the initial configuration is stated:

$$\int_{\Omega_o} D \, d\Omega_o - \int_{\Omega_o} \bar{D} \, d\Omega_o + \oint_{\Gamma_o} l_c^2 \, \mathbf{n}_o \cdot \nabla \bar{D} \, d\Gamma_o = 0 \quad (\text{B5})$$

Given the definition of the volume change  $J$ , the volume in the updated configuration can be related to the initial volume:

$$J_n^{-1} V_u = V_o \quad (\text{B6})$$

where  $J_n$  is the volume change from the previous time step. Nanson's formula is employed to describe the updated  $\Gamma_u$  area vector in terms of the initial area vector  $\Gamma_o$ :

$$\boldsymbol{\Gamma}_u = J_n \mathbf{F}_n^{-T} \cdot \boldsymbol{\Gamma}_0 \quad (\text{B7})$$

The initial area vector  $\Gamma_o$  can then be rewritten in terms of the updated area vector  $\Gamma_u$ :

$$J_n^{-1} \mathbf{F}_n^T \cdot \boldsymbol{\Gamma}_u = \boldsymbol{\Gamma}_0 \quad (\text{B8})$$

Using equation B6, the first two volume integral terms in equation B8 can be given in terms of the updated configuration as:

$$\int_{\Omega_o} D \, d\Omega_o = \int_{\Omega_u} J_n^{-1} D \, d\Omega_u \quad (\text{B9})$$

$$\int_{\Omega_o} \bar{D} \, d\Omega_o = \int_{\Omega_u} J_n^{-1} \bar{D} \, d\Omega_u \quad (\text{B10})$$

Gauss' theorem can then be used to reformulate the gradient term within the third term of equation B5:

$$\oint_{\Gamma_o} l_c^2 \, \mathbf{n}_o \cdot \nabla \bar{D} \, d\Gamma_o = \oint_{\Gamma_o} l_c^2 \, \mathbf{n}_o \cdot \left( \oint_{\Gamma_o} \mathbf{n}_o \bar{D} \, d\Gamma_o \right) d\Gamma_o \quad (\text{B11})$$

The term on the right-hand side of equation B11 can then be reformulated in terms of the updated configuration by combining it with equation B8 to give

The full equation to be solved is therefore

### Algorithmic approach

Equation ?? is solved as shown in equation B12, with the second and third terms added in to aid with convergence. The divergence, gradient and Laplacian terms are discretised using the Gauss linear scheme [37]. A user-defined number of outer iterations are performed around this equation. The code for its implementation is provided in Appendix C.

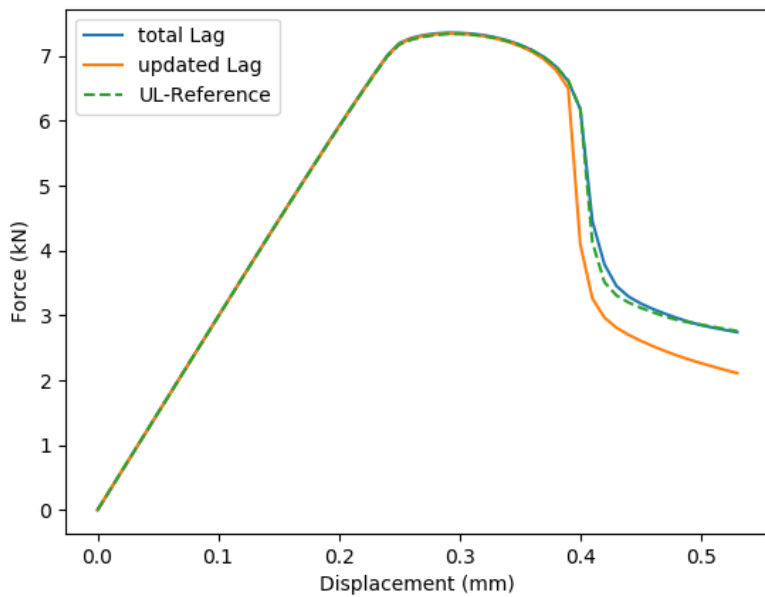
$$\begin{aligned}
& \underbrace{\int_{\Omega_u} J_n^{-1} \bar{D} \, d\Omega_u}_{\text{implicit}} - \underbrace{\oint_{\Gamma_u} \mathbf{n}_u \cdot \nabla (\Delta \bar{D}) \, d\Gamma_u}_{\text{implicit}} \\
& + \underbrace{\oint_{\Gamma_u} \mathbf{n}_u \cdot \nabla (\Delta \bar{D}) \, d\Gamma_u}_{\text{explicit}} \\
& - \underbrace{\oint_{\Gamma_u} l_c^2 (J_n^{-1} \mathbf{F}_n^T \cdot \mathbf{n}_u) \cdot \left( \oint_{\Gamma_u} (J_n^{-1} \mathbf{F}_n^T \cdot \mathbf{n}_u) \bar{D} \, d\Gamma_u \right) \, d\Gamma_u}_{\text{explicit}} \\
& = \underbrace{\int_{\Omega_u} J_n^{-1} \bar{D} \, d\Omega_u}_{\text{explicit}}
\end{aligned} \tag{B12}$$

## B.1 Validation of updated-Lagrangian to reference approach

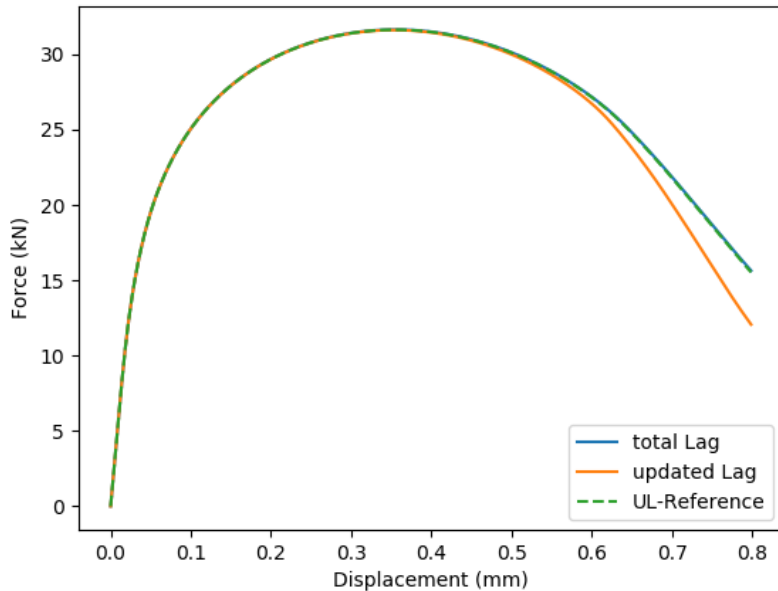
In this section, the implementation of the approach described in section ?? is verified. This is done by simulating each of case a and case b (from section 4.4.5) in the following three ways

- With an updated Lagrangian solid model
- With a total Lagrangian solid model
- with an updated Lagrangian solid model and the non-local damage gradient equation solved with respect to the initial configuration

The force-displacement curves for these simulations are given in Figure B8. The results of the UL to reference approach and the total Lagrangian approach line up well. However, in Figure 6.17 a, a slight discrepancy can be observed which given that very fine time-steps and meshes are used for these simulations is unrelated to discretisation error (Appendix A.1). Is unclear why this exists. It may be due to slight differences in the discretisation techniques - in the UL to reference approach the divergence of the gradient of the non-local damage variable  $\bar{D}$  is solved for, whereas in the total Lagrangian approach the option in OpenFOAM to solve the Laplacian directly is used. Some differences in the Rhie-Chow effects between the total-Lagrangian and updated-Lagrangian approach may also contribute.



(a) Flat notched bar - case a



(b) Notched round bar - case b

**Fig. B8** Comparison of approaches

## References

- [1] Riccio, A. (ed.): Damage Growth in Aerospace Composites, 1st ed. 2015 edn. Springer Aerospace Technology. Springer, Cham (2015). <https://doi.org/10.1007/978-3-319-04004-2>
- [2] Johnson, A.F., Toso-Pentecôte, N., Schueler, D.: Numerical modelling of impact and

damage tolerance in aerospace composite structures. In: Numerical Modelling of Failure in Advanced Composite Materials, pp. 479–506. Elsevier, ??? (2015). <https://doi.org/10.1016/B978-0-08-100332-9.00018-9> . <https://linkinghub.elsevier.com/retrieve/pii/B9780081003329000189> Accessed 2022-12-06

- [3] Alharbi, K., Ghadbeigi, H., Efthymiadis, P., Zanganeh, M., Celotto, S., Dashwood, R., Pinna, C.: Damage in dual phase steel DP1000 investigated using digital image correlation and microstructure simulation. *Modelling and Simulation in Materials Science and Engineering* **23**(8), 085005 (2015) <https://doi.org/10.1088/0965-0393/23/8/085005> . Accessed 2022-12-06
- [4] Sirinakorn, T., Uthaisangsuk, V., Srivannasawpal, S.: Microstructure based Description of Deformation Behavior of Dual Phase Steel Sheets. *Procedia Engineering* **81**, 1366–1371 (2014) <https://doi.org/10.1016/j.proeng.2014.10.158> . Accessed 2022-12-06
- [5] Sarraf, I.S.: Meso-Scale Modelling of Deformation, Damage and Failure in Dual Phase Steels. PhD thesis, University of Windsor (2017)
- [6] Uthaisangsuk, V., Prahl, U., Bleck, W.: Characterisation of formability behaviour of multi-phase steels by micromechanical modelling. *International Journal of Fracture* **157**(1-2), 55–69 (2009) <https://doi.org/10.1007/s10704-009-9329-4> . Accessed 2022-12-06
- [7] Chen, Y.: Modeling of Ductile Fracture Using Local Approach : Reliable Simulation of Crack Extension. PhD thesis, École des Mines de Paris (2020)
- [8] Masse, T.: Study and Optimization of High Carbon Steel Flat Wires. PhD thesis, École des Mines de Paris (2010)
- [9] Cao, T.S.: Models for ductile damage and fracture prediction in cold bulk metal forming processes: a review. *International Journal of Material Forming* **10**(2), 139–171 (2017) <https://doi.org/10.1007/s12289-015-1262-7> . Accessed 2022-12-06
- [10] Tekkaya, A.E., Bouchard, P.-O., Bruschi, S., Tasan, C.C.: Damage in metal forming. *CIRP Annals* **69**(2), 600–623 (2020) <https://doi.org/10.1016/j.cirp.2020.05.005> . Accessed 2022-12-06
- [11] Clancy, M.: Improving the predictive capabilities of wire processing simulations. PhD thesis, University College Dublin (2019)
- [12] Borchers, C., Kirchheim, R.: Cold-drawn pearlitic steel wires. *Progress in Materials Science* **82**, 405–444 (2016) <https://doi.org/10.1016/j.pmatsci.2016.06.001> . Accessed 2023-01-06
- [13] Cardiff, P., Tuković, v., Jaeger, P.D., Clancy, M., Ivanković, A.: A Lagrangian cell-centred finite volume method for metal forming simulation. *International Journal for Numerical Methods in Engineering* **109**(13), 1777–1803 (2017) <https://doi.org/10.1002/nme.5345> . Accessed 2022-10-27
- [14] Besson, J.: Continuum Models of Ductile Fracture: A Review. *International Journal of Damage Mechanics* **19**(1), 3–52 (2010) <https://doi.org/10.1177/1056789509103482> . Accessed 2022-01-13

- [15] Sumpter, J.: An Experimental Investigation of the. In: Hackett, E., Schwalbe, K.-H., Dodds, R. (eds.) Constraint Effects in Fracture, pp. 492–49211. ASTM International, 100 Barr Harbor Drive, PO Box C700, West Conshohocken, PA 19428-2959 (1993). <https://doi.org/10.1520/STP18042S> . <http://www.astm.org/doiLink.cgi?STP18042S> Accessed 2022-01-13
- [16] O'Dowd, N.P., Shih, C.F.: Family of crack-tip fields characterized by a triaxiality parameter—I. Structure of fields. *Journal of the Mechanics and Physics of Solids* **39**(8), 989–1015 (1991) [https://doi.org/10.1016/0022-5096\(91\)90049-T](https://doi.org/10.1016/0022-5096(91)90049-T) . Accessed 2022-01-13
- [17] James, M.A., Newman, J.C.: The effect of crack tunneling on crack growth: experiments and CTOA analyses. *Engineering Fracture Mechanics* **70**(3-4), 457–468 (2003) [https://doi.org/10.1016/S0013-7944\(02\)00131-5](https://doi.org/10.1016/S0013-7944(02)00131-5) . Accessed 2022-01-13
- [18] Mahmoud, S., Lease, K.: The effect of specimen thickness on the experimental characterization of critical crack-tip-opening angle in 2024-T351 aluminum alloy. *Engineering Fracture Mechanics* **70**(3-4), 443–456 (2003) [https://doi.org/10.1016/S0013-7944\(02\)00130-3](https://doi.org/10.1016/S0013-7944(02)00130-3) . Accessed 2022-01-13
- [19] Lemaitre, J.: A Continuous Damage Mechanics Model for Ductile Fracture. *Journal of Engineering Materials and Technology* **107**(1), 83–89 (1985) <https://doi.org/10.1115/1.3225775> . Accessed 2022-01-13
- [20] Lemaître, J., Desmorat, R.: *Engineering Damage Mechanics: Ductile, Creep, Fatigue and Brittle Failures*. Springer, Berlin ; New York (2005). OCLC: ocm56646827
- [21] Gurson, A.L.: Continuum Theory of Ductile Rupture by Void Nucleation and Growth: Part I—Yield Criteria and Flow Rules for Porous Ductile Media. *Journal of Engineering Materials and Technology* **99**(1), 2–15 (1977) <https://doi.org/10.1115/1.3443401> . Accessed 2022-01-13
- [22] Tvergaard, V., Needleman, A.: Analysis of the cup-cone fracture in a round tensile bar. *Acta Metallurgica* **32**(1), 157–169 (1984) [https://doi.org/10.1016/0001-6160\(84\)90213-X](https://doi.org/10.1016/0001-6160(84)90213-X) . Accessed 2022-01-13
- [23] Ambati, M., Gerasimov, T., De Lorenzis, L.: Phase-field modeling of ductile fracture. *Computational Mechanics* **55**(5), 1017–1040 (2015) <https://doi.org/10.1007/s00466-015-1151-4> . Accessed 2022-01-13
- [24] Borden, M.J., Hughes, T.J.R., Landis, C.M., Anvari, A., Lee, I.J.: A phase-field formulation for fracture in ductile materials: Finite deformation balance law derivation, plastic degradation, and stress triaxiality effects. *Computer Methods in Applied Mechanics and Engineering* **312**, 130–166 (2016) <https://doi.org/10.1016/j.cma.2016.09.005> . Accessed 2022-01-13
- [25] Miehe, C., Aldakheel, F., Raina, A.: Phase field modeling of ductile fracture at finite strains: A variational gradient-extended plasticity-damage theory. *International Journal of Plasticity* **84**, 1–32 (2016) <https://doi.org/10.1016/j.ijplas.2016.04.011> . Accessed 2022-01-13
- [26] Dittmann, M., Aldakheel, F., Schulte, J., Wriggers, P., Hesch, C.: Variational phase-field formulation of non-linear ductile fracture. *Computer Methods in Applied Mechanics and*

Engineering **342**, 71–94 (2018) <https://doi.org/10.1016/j.cma.2018.07.029> . Accessed 2022-12-08

- [27] Samaniego, C., Ulloa, J., Rodríguez, P., Houzeaux, G., Vázquez, M., Samaniego, E.: A phase-field model for ductile fracture with shear bands: A parallel implementation. International Journal of Mechanical Sciences **200**, 106424 (2021) <https://doi.org/10.1016/j.ijmecsci.2021.106424> . Accessed 2022-12-08
- [28] Cardiff, P., Demirdžić, I.: Thirty Years of the Finite Volume Method for Solid Mechanics. Archives of Computational Methods in Engineering **28**(5), 3721–3780 (2021) <https://doi.org/10.1007/s11831-020-09523-0> . Accessed 2022-10-27
- [29] Cardiff, P., Karac, A., Jaeger, P.D., Jasak, H., Nagy, J., Ivanković, A., Tuković: An open-source finite volume toolbox for solid mechanics and fluid-solid interaction simulations (2018) <https://doi.org/10.48550/arXiv.1808.10736> . <https://arxiv.org/abs/1808.10736>
- [30] Tuković, Karač, A., Cardiff, P., Jasak, H., Ivanković, A.: Openfoam finite volume solver for fluid-solid interaction. Transactions of FAMENA **42**(3), 1–31 (2018) <https://doi.org/10.21278/TOF.42301>
- [31] Bathe, K.-J.: Finite Element Procedures. Prentice Hall, Englewood Cliffs, N.J (1996)
- [32] Cardiff, P., Tuković, v., Jasak, H., Ivanković, A.: A block-coupled Finite Volume methodology for linear elasticity and unstructured meshes. Computers & Structures **175**, 100–122 (2016) <https://doi.org/10.1016/j.compstruc.2016.07.004> . Accessed 2022-12-08
- [33] Jasak, H., Weller, H.G.: Application of the finite volume method and unstructured meshes to linear elasticity. International Journal for Numerical Methods in Engineering **48**(2), 267–287 (2000) [https://doi.org/10.1002/\(SICI\)1097-0207\(20000520\)48:2\(267::AID-NME884\)3.0.CO;2-Q](https://doi.org/10.1002/(SICI)1097-0207(20000520)48:2(267::AID-NME884)3.0.CO;2-Q) . Accessed 2022-02-08
- [34] Demirdžić, I., Martinović, D.: Finite volume method for thermo-elasto-plastic stress analysis. Computer Methods in Applied Mechanics and Engineering **109**(3-4), 331–349 (1993) [https://doi.org/10.1016/0045-7825\(93\)90085-C](https://doi.org/10.1016/0045-7825(93)90085-C) . Accessed 2022-10-27
- [35] Cardiff, P., Karač, A., FitzPatrick, D., Flavin, R., Ivanković, A.: Development of a Hip Joint Model for Finite Volume Simulations. Journal of Biomechanical Engineering **136**(1), 011006 (2014) <https://doi.org/10.1115/1.4025776> . Accessed 2022-12-08
- [36] Cardiff, P., Karač, A., Ivanković, A.: A large strain finite volume method for orthotropic bodies with general material orientations. Computer Methods in Applied Mechanics and Engineering **268**, 318–335 (2014) <https://doi.org/10.1016/j.cma.2013.09.008> . Accessed 2022-12-09
- [37] OpenFOAM: OpenFOAM Programmer's Guide (2015)
- [38] Cardiff, P., Karač, A., Ivanković, A.: Development of a finite volume contact solver based on the penalty method. Computational Materials Science **64**, 283–284 (2012) <https://doi.org/10.1016/j.commatsci.2012.03.011> . Accessed 2022-10-27

- [39] Batistić, I., Cardiff, P., Tuković: A finite volume penalty based segment-to-segment method for frictional contact problems. *Applied Mathematical Modelling* **101**, 673–693 (2022) <https://doi.org/10.1016/j.apm.2021.09.009>
- [40] Batistić, I., Cardiff, P., Ivanković, A., Tuković, v.: A finite volume penalty-based implicit procedure for the treatment of the frictionless contact boundaries. *International Journal for Numerical Methods in Engineering* **124**(18), 4171–4191 (2023)
- [41] Rhee, C.M., Chow, W.L.: Numerical study of the turbulent flow past an airfoil with trailing edge separation. *AIAA Journal* **21**(11), 1525–1532 (1983) <https://doi.org/10.2514/3.8284> . Accessed 2022-12-01
- [42] Demirdžić, I., Muzaferija, S.: Numerical method for coupled fluid flow, heat transfer and stress analysis using unstructured moving meshes with cells of arbitrary topology. *Computer Methods in Applied Mechanics and Engineering* **125**(1-4), 235–255 (1995) [https://doi.org/10.1016/0045-7825\(95\)00800-G](https://doi.org/10.1016/0045-7825(95)00800-G) . Accessed 2022-02-03
- [43] Bijelonja, I.: Finite volume method for incremental analysis of small and large thermo-elasto-plastic deformations. PhD thesis, University of Sarajevo (2002). In Bosnian
- [44] Bijelonja, I., Demirdžić, I., Muzaferija, S.: A finite volume method for large strain analysis of incompressible hyperelastic materials. *International Journal for Numerical Methods in Engineering* **64**, 1594–1609 (2005)
- [45] Bijelonja, I.: FINITE VOLUME METHOD ANALYSIS OF LARGE STRAIN ELASTO-PLASTIC DEFORMATION. In: The 16<sup>th</sup> DAAAM International Symposium, Opatia, Croatia (2005)
- [46] Bijelonja, I., Demirdžić, I., Muzaferija, S.: A finite volume method for incompressible linear elasticity. *Computer Methods in Applied Mechanics and Engineering* **195**, 6378–6390 (2006)
- [47] Jacobs, D.A.H.: A Generalization of the Conjugate-Gradient Method to Solve Complex Systems. *IMA Journal of Numerical Analysis* **6**(4), 447–452 (1986) <https://doi.org/10.1093/imanum/6.4.447> . Accessed 2022-10-28
- [48] Karypis, G., Kumar, V.: A fast and highly quality multilevel scheme for partitioning irregular graphs. *SIAM Journal on Scientific Computing* **20**(1), 359–392 (1999)
- [49] Pellegrini, F.: Scotch and PT-Scotch Graph Partitioning Software: An Overview. In: Uwe Naumann, O.S. (ed.) *Combinatorial Scientific Computing*, pp. 373–406. Chapman and Hall/CRC, ??? (2012). <https://doi.org/10.1201/b11644-15> . <https://inria.hal.science/hal-00770422>
- [50] Garrison, W.M., Moody, N.R.: Ductile fracture. *Journal of Physics and Chemistry of Solids* **48**(11), 1035–1074 (1987) [https://doi.org/10.1016/0022-3697\(87\)90118-1](https://doi.org/10.1016/0022-3697(87)90118-1) . Accessed 2023-01-05
- [51] Bai, Y., Wierzbicki, T.: A new model of metal plasticity and fracture with pressure and Lode dependence. *International Journal of Plasticity* **24**(6), 1071–1096 (2008) <https://doi.org/10>.

[1016/j.ijplas.2007.09.004](https://doi.org/10.1016/j.ijplas.2007.09.004) . Accessed 2022-03-11

- [52] Nahshon, K., Hutchinson, J.W.: Modification of the Gurson Model for shear failure. European Journal of Mechanics - A/Solids **27**(1), 1–17 (2008) <https://doi.org/10.1016/j.euromechsol.2007.08.002> . Accessed 2022-03-11
- [53] Eterovic, A.L., Bathe, K.-J.: A hyperelastic-based large strain elasto-plastic constitutive formulation with combined isotropic-kinematic hardening using the logarithmic stress and strain measures. International Journal for Numerical Methods in Engineering **30**(6), 1099–1114 (1990) <https://doi.org/10.1002/nme.1620300602> . Accessed 2023-01-05
- [54] Koji, M., Bathe, K.-J.: Inelastic Analysis of Solids and Structures. Springer, Berlin; [London (2010). OCLC: 781682619
- [55] Souza Neto, E.A., Peri, D., Owen, D.R.J.: Computational Methods for Plasticity. John Wiley & Sons, Ltd, Chichester, UK (2008). <https://doi.org/10.1002/9780470694626> . <http://doi.wiley.com/10.1002/9780470694626> Accessed 2022-01-13
- [56] Caminero, M.A., Montáns, F.J., Bathe, K.-J.: Modeling large strain anisotropic elasto-plasticity with logarithmic strain and stress measures. Computers & Structures **89**(11-12), 826–843 (2011) <https://doi.org/10.1016/j.compstruc.2011.02.011> . Accessed 2022-11-23
- [57] Simo, J.C., Hughes, T.J.R.: Computational Inelasticity. Interdisciplinary applied mathematics, vol. v. 7. Springer, New York (1998)
- [58] Bouchard, P.-O., Bourgeon, L., Fayolle, S., Mocellin, K.: An enhanced Lemaitre model formulation for materials processing damage computation. International Journal of Material Forming **4**(3), 299–315 (2011) <https://doi.org/10.1007/s12289-010-0996-5> . Accessed 2022-12-11
- [59] Malcher, L., Mamiya, E.N.: An improved damage evolution law based on continuum damage mechanics and its dependence on both stress triaxiality and the third invariant. International Journal of Plasticity **56**, 232–261 (2014) <https://doi.org/10.1016/j.ijplas.2014.01.002> . Accessed 2022-12-10
- [60] Ferreira, G., Campos, E., Neves, R., Desmorat, R., Malcher, L.: An improved continuous damage model to estimate multiaxial fatigue life under strain control problems. International Journal of Damage Mechanics **31**(6), 815–844 (2022) <https://doi.org/10.1177/10567895221091306> . Accessed 2022-12-15
- [61] Castro, F., Bemfica, C.: Calibration and evaluation of the Lemaitre damage model using axial- torsion fatigue tests on five engineering alloys. Latin American Journal of Solids and Structures **15**(10) (2018) <https://doi.org/10.1590/1679-78254340> . Accessed 2022-12-15
- [62] Ko, Y.K., Lee, J.S., Huh, H., Kim, H.K., Park, S.H.: Prediction of fracture in hub-hole expanding process using a new ductile fracture criterion. Journal of Materials Processing Technology **187-188**, 358–362 (2007) <https://doi.org/10.1016/j.jmatprotec.2006.11.071> . Accessed 2022-12-11

- [63] Roh, Y.-H., Cho, D., Choi, H.-C., Yang, Z., Lee, Y.: Process Condition Diagram Predicting Onset of Microdefects and Fracture in Cold Bar Drawing. *Metals* **11**(3), 479 (2021) <https://doi.org/10.3390/met11030479> . Accessed 2022-12-10
- [64] Bao, Y., Wierzbicki, T.: On the cut-off value of negative triaxiality for fracture. *Engineering Fracture Mechanics* **72**(7), 1049–1069 (2005) <https://doi.org/10.1016/j.engfracmech.2004.07.011> . Accessed 2022-10-11
- [65] Chu, C.C., Needleman, A.: Void Nucleation Effects in Biaxially Stretched Sheets. *Journal of Engineering Materials and Technology* **102**(3), 249–256 (1980) <https://doi.org/10.1115/1.3224807> . Accessed 2022-01-13
- [66] Teixeira, P.M.C.: Ductile Damage Prediction in Sheet Metal Forming and Experimental Validation. PhD thesis, Faculdade de Engenharia da Universidade do Porto (2010)
- [67] Basic, H., Demirdžić, I., Muzaferija, S.: Finite volume method for simulation of extrusion processes. *International Journal for Numerical Methods in Engineering* **62**(4), 475–494 (2005) <https://doi.org/10.1002/nme.1168> . Accessed 2022-12-08
- [68] Pires, F.M.A.: Issues on the Finite Element Modelling of Degradation and Prediction of Failure in Finitely Straining Ductile Materials. PhD thesis, University of Wales Swansea (2005)
- [69] Desmorat, R., Cantournet, S.: Modeling Microdefects Closure Effect with Isotropic/Anisotropic Damage. *International Journal of Damage Mechanics* **17**(1), 65–96 (2008) <https://doi.org/10.1177/1056789507069541> . Accessed 2022-12-11
- [70] Lemaitre, J.: A Course on Damage Mechanics, 2., rev. and enlarged ed edn. Springer, Berlin (1996)
- [71] Peerlings, R.H.J., Geers, M.G.D., Borst, R., Brekelmans, W.A.M.: A critical comparison of nonlocal and gradient-enhanced softening continua. *International Journal of Solids and Structures* **38**(44-45), 7723–7746 (2001) [https://doi.org/10.1016/S0020-7683\(01\)00087-7](https://doi.org/10.1016/S0020-7683(01)00087-7) . Accessed 2022-12-05
- [72] Peerlings, R.H.J., de Borst, R., Brekelmans, W.A.M., Geers, M.G.D.: Localisation issues in local and nonlocal continuum approaches to fracture. *European Journal of Mechanics - A/Solids* **21**(2), 175–189 (2002) [https://doi.org/10.1016/S0997-7538\(02\)01211-1](https://doi.org/10.1016/S0997-7538(02)01211-1) . Accessed 2022-01-13
- [73] Geers, M.G.D., Ubachs, R.L.J.M., Engelen, R.A.B.: Strongly non-local gradient-enhanced finite strain elastoplasticity. *International Journal for Numerical Methods in Engineering* **56**(14), 2039–2068 (2003) <https://doi.org/10.1002/nme.654> . Accessed 2022-01-13
- [74] Bettaieb, M.B., Lemoine, X., Duchêne, L., Habraken, A.M.: On the numerical integration of an advanced Gurson model. *International Journal for Numerical Methods in Engineering* **85**(8), 1049–1072 (2011) <https://doi.org/10.1002/nme.3010> . Accessed 2023-01-06
- [75] Achouri, M., Germain, G., Dal Santo, P., Saidane, D.: Numerical integration of an advanced

Gurson model for shear loading: Application to the blanking process. Computational Materials Science **72**, 62–67 (2013) <https://doi.org/10.1016/j.commatsci.2013.01.035> . Accessed 2023-01-06

- [76] Malcher, L.: Continuum Modelling and Numerical Simulation of Damage for Ductile Materials. PhD, University of Porto (2012)
- [77] Leclerc, J., Nguyen, V.-D., Pardoen, T., Noels, L.: A micromechanics-based non-local damage to crack transition framework for porous elastoplastic solids. International Journal of Plasticity **127**, 102631 (2020) <https://doi.org/10.1016/j.ijplas.2019.11.010> . Accessed 2023-01-06
- [78] Reusch, F., Svendsen, B., Klingbeil, D.: A non-local extension of Gurson-based ductile damage modeling. Computational Materials Science **26**, 219–229 (2003) [https://doi.org/10.1016/S0927-0256\(02\)00402-0](https://doi.org/10.1016/S0927-0256(02)00402-0) . Accessed 2023-01-06
- [79] Borden, M.J., Verhoosel, C.V., Scott, M.A., Hughes, T.J.R., Landis, C.M.: A phase-field description of dynamic brittle fracture. Computer Methods in Applied Mechanics and Engineering **217-220**, 77–95 (2012) <https://doi.org/10.1016/j.cma.2012.01.008> . Accessed 2022-01-13
- [80] Miehe, C., Hofacker, M., Welschinger, F.: A phase field model for rate-independent crack propagation: Robust algorithmic implementation based on operator splits. Computer Methods in Applied Mechanics and Engineering **199**(45-48), 2765–2778 (2010) <https://doi.org/10.1016/j.cma.2010.04.011> . Accessed 2022-01-13
- [81] Francfort, G.A., Marigo, J.-J.: Revisiting brittle fracture as an energy minimization problem. Journal of the Mechanics and Physics of Solids **46**(8), 1319–1342 (1998) [https://doi.org/10.1016/S0022-5096\(98\)00034-9](https://doi.org/10.1016/S0022-5096(98)00034-9) . Accessed 2022-03-16
- [82] Mumford, D., Shah, J.: Optimal approximations by piecewise smooth functions and associated variational problems. Communications on Pure and Applied Mathematics **42**(5), 577–685 (1989) <https://doi.org/10.1002/cpa.3160420503> . Accessed 2022-03-16
- [83] Ambrosio, L., Tortorelli, V.M.: Approximation of functional depending on jumps by elliptic functional via t-convergence. Communications on Pure and Applied Mathematics **43**(8), 999–1036 (1990) <https://doi.org/10.1002/cpa.3160430805> . Accessed 2022-03-16
- [84] Bourdin, B., Larsen, C.J., Richardson, C.L.: A time-discrete model for dynamic fracture based on crack regularization. International Journal of Fracture **168**(2), 133–143 (2011) <https://doi.org/10.1007/s10704-010-9562-x> . Accessed 2023-01-03
- [85] Amor, H., Marigo, J.-J., Maurini, C.: Regularized formulation of the variational brittle fracture with unilateral contact: Numerical experiments. Journal of the Mechanics and Physics of Solids **57**(8), 1209–1229 (2009) <https://doi.org/10.1016/j.jmps.2009.04.011> . Accessed 2022-03-22
- [86] Eldahshan, H., Munoz, D.P., Alves, J., Perchat, E., Bouchard, P.-O.: 3D crack initiation and propagation applied to metal forming processes. International Journal of Material Forming

**15**(5), 60 (2022) <https://doi.org/10.1007/s12289-022-01702-7> . Accessed 2023-01-06

- [87] Sá, J.M.A., Areias, P.M.A., Zheng, C.: Damage modelling in metal forming problems using an implicit non-local gradient model. *Computer Methods in Applied Mechanics and Engineering* **195**(48-49), 6646–6660 (2006) <https://doi.org/10.1016/j.cma.2005.02.037> . Accessed 2022-01-13
- [88] Fincato, R., Tsutsumi, S.: A return mapping algorithm for elastoplastic and ductile damage constitutive equations using the subloading surface method. *International Journal for Numerical Methods in Engineering* **113**(11), 1729–1754 (2018) <https://doi.org/10.1002/nme.5718> . Accessed 2022-11-23
- [89] Vaz, M., Owen, D.R.J.: Aspects of ductile fracture and adaptive mesh refinement in damaged elasto-plastic materials. *International Journal for Numerical Methods in Engineering* **50**(1), 29–54 (2001) [https://doi.org/10.1002/1097-0207\(20010110\)50:1<29::AID-NME18>3.0.CO;2-G](https://doi.org/10.1002/1097-0207(20010110)50:1<29::AID-NME18>3.0.CO;2-G) . Accessed 2022-11-23
- [90] Eldahshan, H., Bouchard, P.-O., Alves, J., Perchat, E., Munoz, D.P.: Phase field modeling of ductile fracture at large plastic strains using adaptive isotropic remeshing. *Computational Mechanics* **67**(3), 763–783 (2021) <https://doi.org/10.1007/s00466-020-01962-7> . Accessed 2022-03-22
- [91] Soyarslan, C., Tekkaya, A.E.: Finite deformation plasticity coupled with isotropic damage: Formulation in principal axes and applications. *Finite Elements in Analysis and Design* **46**(8), 668–683 (2010) <https://doi.org/10.1016/j.finel.2010.03.006> . Accessed 2023-03-14
- [92] González, A.A., Celentano, D.J., Cruchaga, M.A.: Assessment of ductile failure models in single-pass wire drawing processes. *International Journal of Damage Mechanics* **27**(9), 1291–1306 (2018) <https://doi.org/10.1177/1056789517704029> . Accessed 2022-12-13
- [93] Norasethasopon, S., Yoshida, K.: Prediction of chevron crack initiation in inclusion copper shaped-wire drawing. *Engineering Failure Analysis* **15**(4), 378–393 (2008) <https://doi.org/10.1016/j.engfailanal.2007.01.003> . Accessed 2023-01-01
- [94] Zimmerman, Z., Darlington, H., Kottcamp, E.H.: Selection of Operating Parameters to Prevent Central Bursting Defects During Cold Extrusion. In: Hoffmanner, A.L. (ed.) *Metal Forming: Interrelation Between Theory And Practice*, pp. 47–62. Springer, Boston, MA (1971). [https://doi.org/10.1007/978-1-4615-1757-3\\_2](https://doi.org/10.1007/978-1-4615-1757-3_2) . [http://link.springer.com/10.1007/978-1-4615-1757-3\\_2](http://link.springer.com/10.1007/978-1-4615-1757-3_2) Accessed 2023-01-01
- [95] Choi, J.-S., Lee, H.-C., Im, Y.-T.: A study on chevron crack formation and evolution in a cold extrusion. *Journal of Mechanical Science and Technology* **24**(9), 1885–1890 (2010) <https://doi.org/10.1007/s12206-010-0605-z> . Accessed 2023-01-01
- [96] Cao, T.-S.: Modelling Ductile Damage for Complex Loading Paths. PhD, École des Mines de Paris (2014)
- [97] Thuillier, S., Maire, E., Brunet, M.: Ductile damage in aluminium alloy thin sheets:

Correlation between micro-tomography observations and mechanical modeling. Materials Science and Engineering: A **558**, 217–225 (2012) <https://doi.org/10.1016/j.msea.2012.07.116> . Accessed 2022-12-10

- [98] Fansi, J., Balan, T., Lemoine, X., Maire, E., Landron, C., Bouaziz, O., Ben Bettaieb, M., Marie Habraken, A.: Numerical investigation and experimental validation of physically based advanced GTN model for DP steels. Materials Science and Engineering: A **569**, 1–12 (2013) <https://doi.org/10.1016/j.msea.2013.01.019> . Accessed 2022-12-10
- [99] Loh, W.-L.: On Latin hypercube sampling. The Annals of Statistics **24**(5) (1996) <https://doi.org/10.1214/aos/1069362310> . Accessed 2022-12-11
- [100] Luersen, M.A., Le Riche, R.: Globalized Nelder–Mead method for engineering optimization. Computers & Structures **82**(23–26), 2251–2260 (2004) <https://doi.org/10.1016/j.compstruc.2004.03.072> . Accessed 2022-12-11
- [101] Liu, X., Liu, Y., Jin, B., Lu, Y., Lu, J.: Microstructure Evolution and Mechanical Properties of a SMATed Mg Alloy under In Situ SEM Tensile Testing. Journal of Materials Science & Technology **33**(3), 224–230 (2017) <https://doi.org/10.1016/j.jmst.2016.11.012> . Accessed 2022-12-20
- [102] Li, H., Fu, M.W., Lu, J., Yang, H.: Ductile fracture: Experiments and computations. International Journal of Plasticity **27**(2), 147–180 (2011) <https://doi.org/10.1016/j.ijplas.2010.04.001> . Accessed 2022-12-02
- [103] Krauss, G.: Steels: Processing, Structure, and Performance, Second edition edn. ASM International, Materials Park, Ohio (2015). OCLC: ocn904652440
- [104] Azinpour, E., Ferreira, J.P.S., Parente, M.P.L., Sa, J.C.: A simple and unified implementation of phase field and gradient damage models. Advanced Modeling and Simulation in Engineering Sciences **5**(1), 15 (2018) <https://doi.org/10.1186/s40323-018-0106-7> . Accessed 2022-11-09
- [105] Cardiff, P.: Patch Test. <https://solids4foam.github.io/tutorials/more-tutorials/solid-mechanics/linearElasticity/patchTest.html>
- [106] Autay, R., Koubaa, S., Wali, M., Dammak, F.: Numerical Implementation of Coupled Anisotropic Plasticity-Ductile Damage in Sheet Metal Forming Process. Journal of Mechanics **34**(4), 417–430 (2018) <https://doi.org/10.1017/jmech.2017.28> . Accessed 2022-11-14
- [107] Doghri, I.: Numerical implementation and analysis of a class of metal plasticity models coupled with ductile damage. International Journal for Numerical Methods in Engineering **38**(20), 3403–3431 (1995) <https://doi.org/10.1002/nme.1620382004> . Accessed 2022-01-13
- [108] Steinmann, P.: Formulation and computation of geometrically non-linear gradient damage. International Journal for Numerical Methods in Engineering, 757–779